Universidade de Aveiro Departamento de Engenharia Cerâmica e do Vidro
2008

EKATERINA SELEZNEVA

MAGNETOELECTRIC COMPOSITES BASED ON HEXAGONAL FERRITES

Universidade de Aveiro Departamento de Engenharia Cerâmica e do Vidro
2008

EKATERINA SELEZNEVA

COMPÓSITOS MAGNETOELECTRICOS BASEADOS EM FERRITES HEXAGONAIS

dissertação apresentada à Universidade de Aveiro para cumprimento dos requisitos necessários à obtenção do grau de Mestre em Ciência e Engenharia de Materiais, realizada sob a orientação científica do Dr. Andrei Kholkine, Investigador Principal do Departamento de Engenharia Cerâmica e do Vidro e do CICECO da Universidade de Aveiro e do Prof. Dr. Gerold Schneider, Professor Associado do Departamento de Cerâmica Avançado da Technische Universität Hamburg-Harburg.

o júri

presidente

Prof. Dr. Vitor Brás de Sequeira Amaral
Professor associado do Departamento de Fisica da Universidade de Aveiro

Dr. Andrei Kholkine
Investigador principal do Departamento de Engenharia Cerâmica e do Vidro da Universidade de Aveiro

Prof. Dr. Yuriy Pogorelov
Professor associado do Departamento de Fisica da Universidade do Porto.

agradecimentos

Dr. A. Kholkine, Investigador Principal, Departamento de Engenharia Cerâmica e do Vidro da U.A, for coordination in theoretical and practical work

Dr. R. C. Pullar, Department of Materials, Imperial College London, for the granted samples

F. G. Figueiras, Departamento de Física da U.A., for collaboration in experimental work by VSM, support in the analysis of the XRD data, and for the general guidance during writing of the dissertation.

I. Bdikin, Departamento de Engenharia Cerâmica e do Vidro da U.A, for the support in experimental work in AFM

Yuri K. Fetisov, Professor & Dean, Faculty of Electroncs, MIREA, for the help with the dielectric measurements

Maria Armanda de Araujo Sa, Assessora Principal, Departamento de Física da Universidade do Porto, for the help in experimental work by VSM

Maria da Conceição Braga dos Anjos Pereira da Costa, técnico especialista principal, Departamento de Engenharia Cerâmica e do Vidro da U.A, for the help with XRD measurements

Kiril Yasakau, Departamento de Engenharia Cerâmica e do Vidro da U.A, for the help with SEM measurements

Eugene Kiselev, Departamento de Engenharia Cerâmica e do Vidro da U.A, for the help with XRD measurements

palavras-chave

Compósitos Magnetoelectricos, ferrites hexagonais, $BaFe_{12}O_{19}$, $SrFe_{12}O_{19}$, $Ba_3Co_2Fe_{24}O_{41}$, $BaTiO_3$.

resumo

Compósitos Magnetoelectricos baseados em ferrites hexagonais $BaFe_{12}O_{19}$, $SrFe_{12}O_{19}$, $Ba_3Co_2Fe_{24}O_{41}$, e em perovsquites ferroelectricas $BaTiO_3$, foram estudadas.

Foram realizadas análises estruturais por difracção de Raios-X e microscopia de varrimento de electrões; ambas as fases, ferroelectrica e ferromagnética apresentam distorções apreciáveis dos parâmetros de rede cristalina.

As propriedades ferroelectricas foram medidas por microscopia de força de resposta piezoelectrica, sendo detectado uma diminuição das propriedades ferroelectricas nos compósitos em comparação com o material $BaTiO_3$ puro.

Medidas magnéticas foram realizadas com magnetometria por vibração da amostra (VSM) e microscopia de força magnética (MFM). As medidas efectuadas por VSM confirmam a proporcionalidade entre a magnetização saturação e a respectiva fracção da fase ferromagnetica em todos os compósitos.

Medidas locais do acoplamento magnetoelectrico foram efectuadas através de microscopia de força atómica, tendo sido detectadas efeitos localizados na magnetização de grãos ferrite contíguos a grãos de $BaTiO_3$ sujeitos a uma inversão da polarização.

keywords

Magnetoelectric composites, $BaFe_{12}O_{19}$, $SrFe_{12}O_{19}$, $Ba_3Co_2Fe_{24}O_{41}$, hexagonal ferrites, $BaTiO_3$

abstract

Magnetoelectric composites based on the hexagonal ferrites $BaFe_{12}O_{19}$, $SrFe_{12}O_{19}$, $Ba_3Co_2Fe_{24}O_{41}$, and the ferroelectric perovskite $BaTiO_3$, were studied.

Structural and phase analysis of the samples was done by X-ray diffraction and scanning electron microscopy. Both ferroelectric and magnetic phases have structural distortion of the unit cell.

Ferroelectic properties were studied by piezoresponse force microscopy. The results show significant worsening of ferroelectric and piezoelectric properties in the composite compared to the pure ferroelectric phase.

Magnetic analyses were done by vibrating sample magnetometry (VSM) and magnetic force microscopy (MFM). The VSM measurements confirmed linear dependence of the magnetization saturation on the fraction of magnetic phase in all of the composites.

The experiment on local electromagnetic coupling was performed by means of atomic force microscopy (AFM). It resulted in a weak effect of polarization switching on the local magnetic properties.

1. INTRODUCTION 3

1.1. MAGNETOELECTRIC COMPOSITES 4

1.1.1. Multiferroic and magnetoelectric materials 4

1.1.2. Historical perspective 5

1.1.3. Theories of bulk ceramic composites 6

1.1.3.1. Phase connectivity 6

1.1.3.2. Effective field theories 7

1.1.4. Properties of magnetoelectric composites 8

1.1.4.1. Magnetic properties 8

1.1.4.2. Dielectric properties 9

1.1.4.3. Magnetoelectric effect 10

1.2. BARIUM TITANATE 11

1.2.1. Crystal Structure 11

1.2.2. Dielectric properties 12

1.2.3. Ferroelectric domains 13

1.3. HEXAGONAL FERRITES 14

1.3.1. M-ferrites 14

1.3.1.1. Crystal and Magnetic structure 14

1.3.1.2. Permanent magnet properties 16

1.3.2. Z-ferrites 17

2. MOTIVATION 19

3. EXPERIMENTAL 20

3.1. SAMPLE PREPARATION 20

3.2. CHARACTERIZATION 21

3.2.1. Structural analysis 21

3.2.1.1. X-ray powder diffraction (XRD) measurement 21

3.2.1.2. Scanning electron microscopy (SEM) 29

3.2.1.3. Energy Dispersive X-Ray Spectrometry (EDS) 30

3.2.2. Dielectric measurements 35

3.2.3. Magnetic measurements 41

3.2.4. Analysis of nanoscale properties 46

3.2.4.1. Piezoresponse force microscopy (PFM) 47
3.2.4.2. Local piezoelectric hysteresis loop acquisition 49
3.2.4.3. Magnetic force microscopy (MFM) 50
3.2.4.4. Local electromagnetic coupling 56

4. RESULTS AND DISCUSSIONS 58

4.1. PHASE DISTRIBUTION 58
4.2. CHANGES IN THE UNIT CELL PARAMETERS 59
4.3. DIELECTRIC PROPERTIES 61
4.4. MAGNETIC PROPERTIES 62
4.5. FERROELECTRIC PROPERTIES 66
4.6. ELECTROMAGNETIC COUPLING 68

5. CONCLUSIONS 69

6. REFERENCES 71

1. INTRODUCTION

The multifunctional materials combining several properties in the same structure in order to produce new or enhanced phenomena have numerous applications and recently stimulated an outstanding scientific and technological interest within the scientific community. Among them, the multiferroics are combining at least two ferroic properties in the same temperature range. The ferroic systems possess an order parameter switchable by an adequate driving force or field, phenomena normally accompanied by hysteresis. Ferroelectrics, ferromagnetics and ferroelastics are typical examples of ferroics. The electric polarization, magnetic moment and strain can be switched from one stable state to another one by means of a sufficiently high electric, magnetic or stress field, respectively.

Although over ten different compound families have been widely investigated as multiferroic magnetoelectric (ME) materials, a high inherent coupling between multiferroic order parameters (especially above room temperature) has not yet been achieved in a single-phase material, which hinders their application. Alternatively and with greater design flexibility, multiferroic ME composites made by combining piezoelectric and magnetic substances together have drawn significant interest in recent years due to their multifunctionality, in which the coupling interaction between piezoelectric and magnetic substances could produce a large ME response (several orders of magnitude higher than that in single-phase ME materials) at room temperature[1].

In present work, magnetoelectric composites based on hexagonal ferrites were studied. Three different compositions were chosen, namely $BaFe_{12}O_{19}$ – $BaTiO_3$, $SrFe_{12}O_{19}$ – $BaTiO_3$, and $Ba_3Co_2Fe_{24}O_{41}$ – $BaTiO_3$. Each of the compositions had two different fractions of the magnetic phase, namely 10 and 50%. The list of the samples is thus presented below:

1) $BaFe_{12}O_{19}$ 10% – $BaTiO_3$ 90%
2) $BaFe_{12}O_{19}$ 50% – $BaTiO_3$ 50%
3) $SrFe_{12}O_{19}$ 10% – $BaTiO_3$ 90%
4) $SrFe_{12}O_{19}$ 50% – $BaTiO_3$ 50%
5) $Ba_3Co_2Fe_{24}O_{41}$ 10% – $BaTiO_3$ 90%
6) $Ba_3Co_2Fe_{24}O_{41}$ 10% – $BaTiO_3$ 90%

The pure phases of $BaFe_{12}O_{19}$, $SrFe_{12}O_{19}$, $Ba_3Co_2Fe_{24}O_{41}$, and $BaTiO_3$ were investigated as a reference.

1.1.Magnetoelectric composites

1.1.1. Multiferroic and magnetoelectric materials

Studies of magnetoelectric materials involve such terms as 'multiferroic' and 'magnetoelectric' that is not equivalent. By the original definition, a single-phase multiferroic[2] material is one that possesses two – or all three – of the so-called 'ferroic' properties: ferroelectricity, ferromagnetism and ferroelasticity. Magnetoelectric coupling, on the other hand, may exist whatever the nature of magnetic and electrical order parameters, and can for example occur in paramagnetic ferroelectrics[3]

The diagram presented in Fig. 1 gives the relationship between these two types of phenomena. Ferromagnets (ferroelectrics) form a subset of magnetically (electrically) polarizable materials such as paramagnets and antiferromagnets (paraelectrics and antiferroelectrics). The intersection (blue hatching) represents materials that are multiferroic. Magnetoelectric coupling (green) is an independent phenomenon that can, but need not, arise in any of the materials that are both magnetically and electrically polarizable[4].

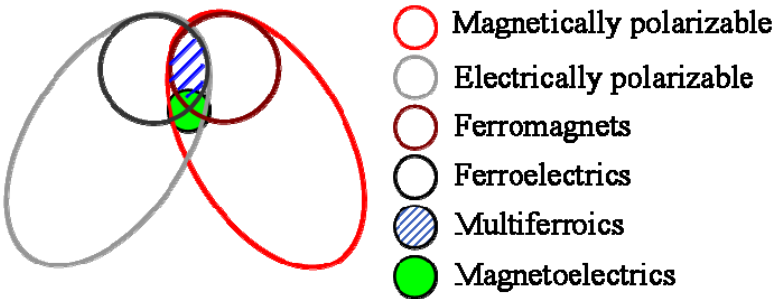

Fig 1. *The relationship between multiferroic and magnetoelectric materials*

In practice, there are very few 'multiferroic' materials that exhibit both of these properties, but the 'magnetoelectric' coupling of magnetic and electrical properties is a more general and widespread phenomenon

1.1.2. Historical perspective

The idea of synthesizing a composite medium displaying a ME effect was first formulated by Tellegen in 1948[5], that is more than a decade before the first observation of intrinsic ME behavior in a single phase compound. Tellegen suggested a suspension of microscopic particles that carry both electric and magnetic dipole moments, an idea, that, however, has not been realized.

In 1972 van Suchtelen proposed the concept of a product property in two-phase composite materials, arising from an elastic coupling between two phases of different properties[6]. If a system is formed by more than one phase, its functional properties result as being derived both by the properties of the constituents and also by their mutual interactions (synergy effects). In this sense, three classes of synergy effects can be identified:

1) *Sum property*, which represents the weighted sum of the components' contributions of the constituent phases (normally the composite's property is less intense than in the parent phases, i.e. dilution effect). Physical quantities like density and resistivity are normally sum properties.
2) *Combination property*, denoting an effect in which, at specific compositions or under specific circumstances, the amplitude of the property is higher in the composite than in the end compounds.
3) *Product property,* referring to effects in the composites but not in the individual phases. Whereas the sum and combination properties are describing average or enhancement of effects already present in the parent phases, the product property only refers to novel phenomena originated from the mutual interaction between the individual phases.

Soon after the product ME property in the composite combining magnetostrictive and piezoelectric phases was proposed, scientists in Philips Laboratory experimentally found that the large ME effect could be produced in such composites. They prepared ceramic composites of $BaTiO_3$ – $CoFe_2O_4$ by unidirectional solidification of eutectic compositions in the quinary Fe-Co-Ti-Ba-O system. The magnetoelectric effect obtained in this way can reach about hundred times larger than that in single-phase multiferroic one. But unidirectional solidification is complex and requires critical control over composition and processing. At that time, ME composite research went dormant for almost 20 years across the world. Then in 1990s, Newnham's group and Russian scientists[7,8] prepared particulate ceramic composites of ferrites and $BaTiO_3$ or $Pb(Zr,Ti)O_3$ (PZT) by a conventional sintering processing. The sintered ceramic composites were much easier and cost effective to fabricate in comparison to eutectic composites; and in additional provided the opportunity to combine phases with widely different

crystal structures. However, these sintered ceramic composites had lower ME coefficients than the prior eutectic composites by Philips. Although experimental studies of those ME composites in the 1990s did not represent a great step forward, the experiments did inspire significant theoretical work on ME ceramic composites.

A milestone in the development of ME bulk composites was the fabrication of those containing giant magnetostrictive rare-earth-iron alloy $Tb_{1-x}Dy_xFe_2$ (Terfenol-D) in 2001. It was predicted that both particulate composites with Terfenol-D embedded in a piezoelectric polymer such as poly(vinylidene fluoride-trifluorethylene) co-polymer [P(VDF-TrFE)] or a piezoelectric ceramic matrix, such as PZT, and laminate composites of Terfenol-D/P(VDF-TrFE) or Terfenol-D/PZT, could exhibit a giant ME (GME) effect. Subsequently, the laminate Terfenol-D/PZT[9] and Terfenol-D/PVDF[10] composites have been experimentally found to exhibit such GME effect.

Recently, in order to overcome brittleness and high eddy current loss in Terfenol-D/piezoceramic composites, three phase ME bulk composites of Terfenol-D/piezoceramic/polymer have been developed[11].

1.1.3. Theories of bulk ceramic composites

1.1.3.1. Phase connectivity

In 1978 Newnham *et al.* have introduced the concept of phase connectivity[12]. Each phase in a composite may be self-connected in zero, one, two, or three dimensions. It is natural to confine attention to three perpendicular axes because all property tensors are referred to such systems. In the case of two-phase composites, there are ten connectivities: 0-0, 1-0, 2-0, 3-0, 1-1, 2-1, 3-1, 2-2, 3-2, and 3-3. The ten different connectivities are illustrated in Fig. 2, using a cube as the basic building block. A 2-1 connectivity pattern, for example, has the shaded phase self-connected in two-dimensional layers and the unshaded phase self-connected in one dimensional fibers. The connectivity patterns are not geometrically unique. In the case of a 2-1 pattern the fibers of the unshaded phase might be perpendicular to the layers of the first phase, as seen on Fig. 2, or the might be parallel to the layers.

The most complicated and in many ways the most interesting pattern is 3-3 connectivity in which the two phases form interpenetrating three-dimensional networks. Patterns of this type often occur in living systems such as corals where organic tissue and an inorganic skeleton interpenetrate one into another.

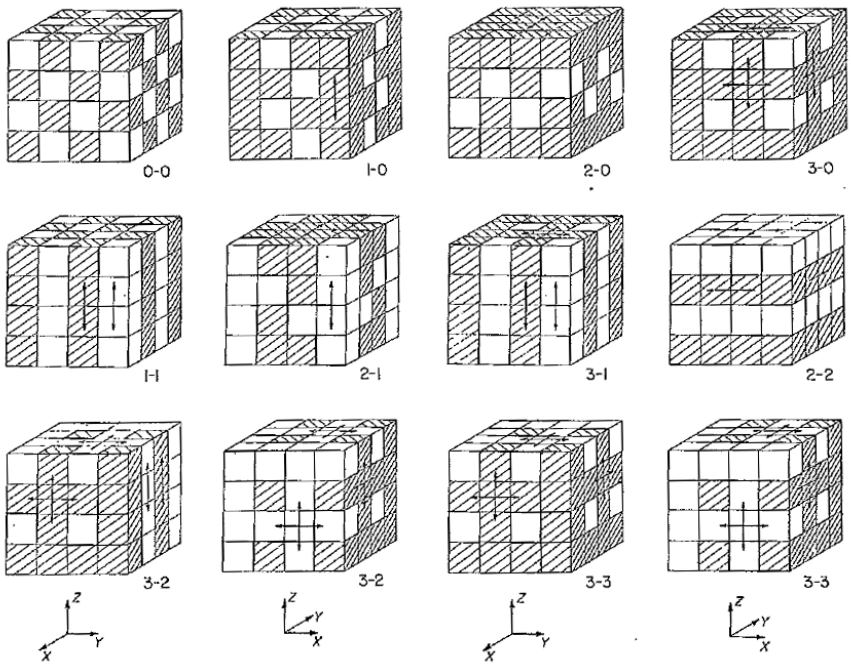

Fig 2. *Ten connectivity patterns for two-phase composites. Arrows are used to indicate the connected directions.*

In the case of magnetoelectric composites, consisted of magnetic (presumably conductive) phase and non-conductive ferroelectric one, the most suitable connectivity schemes are expected to be 3-0, 2-0 or 2-2. In such microstructures, there is a chance to avoid formation of conductivity percolation channels of the magnetic phase decreasing the performance of ferroelectric phase.

1.1.3.2. Effective field theories

The dielectric and magnetic constants in composites are often theoretically described within effective field models[13], related to the particular mixing degree and volume filling of the component phases. The most common approximations are:

- Maxwell-Garnett, corresponding to isolated spherical inclusions embedded in a continuous matrix background valid for small filling concentrations only
- Bruggeman, considering the properties of matrix or host the same as the effective field medium itself, working well in the entire range of compositions and predicting percolation for a filling volume fraction of 1/3

In the present study, the compositions with 50% ferrite fractions exceed the threshold value of 1/3 predicted by the Bruggeman effective field approximations. Therefore, we may

expect lowering resistivity of the composite derived from ferrite conductivity which would make impossible the proper poling of ferroelectric phase.

1.1.4. Properties of magnetoelectric composites

In spite of some common phenomenological properties of ferroic materials (e.g. existence of a non-zero order parameter below a critical temperature, P-E and M-H hysteresis and non-linearity of the permittivity/permeability vs. the electric and magnetic field), which are the "fingerprints" of their ferroic character, the basic physics driving the ferroelectric and magnetic nature is completely different in these two categories of materials[14]. While a short-range order interaction (exchange type) is characteristic for the magnetics, a long-range dipolar order (weaker interaction) is responsible for ferroelectricity. The intrinsic ferroism in a given material is determined by its fundamental interaction characteristics derived from the nature, strength and orientation of its chemical bonds determining the crystalline symmetry, spin configuration and ordering, spin-orbit coupling, etc. Extrinsic phenomena related to some specific microstructural characteristics such as defects, grain boundaries, interfaces, etc can be also important. When forming a composite from a ferroelectric and magnetic material, the presence of the foreign phase is expected to change mainly the long-range interactions. Accordingly, it seems that the intrinsic ferroelectricity in the composite will be more sensitive to the presence of the magnetic phase than the intrinsic magnetism to the addition of ferroelectric phase.

1.1.4.1. Magnetic properties

The magnetic characteristics of the composites follow from the ferrite's properties, which are sensitive to composition, preparation method and sintering conditions. As it was pointed out above, the presence of the non-magnetic phase in composite does not change the nature of the magnetic interactions. The value of the saturation magnetization in composites normally increases with increase of the magnetic phase content (sum property). Such behavior was reported for instance by X. Qi et al[15].

However, magnetic properties can be affected by some particular microstructural features like density, percolation through the magnetic phase or doping of the ferrite with foreign ions, which are hardly controlled in series of compositions. In the work of H. K. Liu *et al.*[16] completely different composition dependence was observed. At some threshold composition around 95% of ferrite content, the saturation magnetization dramatically decreases (around 5 times) compared to the value corresponding to the pure ferrite.

1.1.4.2. Dielectric properties

As a general trend, magnetoelectric composites present multiple temperature dependent relaxations in the frequency range of (1-10^6) Hz[17] and losses above unity strongly increasing with temperature at low frequencies[18]. The permittivity vs. temperature dependence in composites shows an anomaly in a temperature range around the ferro-paraelectric transition of the non-magnetic phase. This is the proof that the ferroelectric character is maintained in the composite. Regularly, this is a broad maximum due to local composition inhomogeneity and stresses causing a broad distribution of the local Curie temperatures. In some composites the maximum may exactly correspond to the ferroelectric Curie temperature[19], whereas in others this temperature may be shifted towards higher[15] or lower temperatures[18].

Various size effects may compromise the properties of ferroelectrics. In the work of V. Buscaglia *et al*.[20] it was shown that the barium titanate samples with grain size above 300 nm exhibit the tetragonal structure of the unit cell, while in the nanocrystalline barium titanate ceramics with grain size of 100 nm and below the unit cell has cubic symmetry.

As it was pointed out above, dielectric properties are very sensitive to the mictostructural characteristics. The high dielectric losses and the multiple relaxations are caused by a poor homogeneity, high porosity determined by the limited sintering temperature and cracks resulting by co-sintering phases with different thermal expansion coefficients. By improving the microstructure, lower dielectric losses can be obtained. However, in most cases the general dielectric relaxations will be still present. Such phenomena, (extrinsic in nature) could be caused in particular by the Maxwell-Wagner effect[21,22]. Charge defects (e.g. A-site vacancies in perovskite ABO_3, space charge electrons, etc.) can migrate in the applied electric field provided the temperature is high enough to ensure some conductivity of the material. These free carriers can then be blocked at the interface between two media of different conductivity and permittivity, leading to the appearance of the interfacial polarization[23]. This is exactly the case of magnetoelectric composites made of dielectric matrix in which inclusions of a more conductive material is embedded.

1.1.4.3. Magnetoelectric effect

The ME effect in composite materials is a product property which results from the cross interaction between different orderings of the two phases in the composite[24]. ME effect is a result of the product of the magnetostrictive effect (magnetic/mechanical effect) in the magnetic phase and the piezoelectric effect (mechanical/electrical effect) in the piezoelectric one, namely

$$ME_H = \frac{\text{magnetic}}{\text{mechanical}} \times \frac{\text{mechanical}}{\text{electrical}}$$

or

$$ME_E = \frac{\text{electrical}}{\text{mechanical}} \times \frac{\text{mechanical}}{\text{magnetic}}$$

and is a coupled electrical and magnetic phenomenon by elastic interaction.

The magnitude of ME effect is normally described by voltage ME coefficient α^E which is defined as:

$$\alpha^E = \frac{\partial E}{\partial H}, \quad (1)$$

where H is the applied magnetic field and E is induced electric field as a result of the ME coupling. The direction of the generated electric field is determined by the orientation of the ferroelectric domains in the piezoelectric phase that is random without poling. Thus, the alignment of the electric dipoles normally realized by the poling process is essential in order to achieve a substantial ME coupling.

Being determined by a kind of electrical measurement, the ME effect is strongly influenced by the same parameters determining the electric properties of ferroelectric component.

In some cases the increasing volume fraction of the ferrite phase lead to an increase in ME output[25]. This is caused by the increasing magnetostrictively induced strain within the ferrite fraction. Further increase of the ferrite addition caused a reduction of ME coefficient, in spite the magnetostrictively-induced strain still increasing with the ferrite fraction. Such drop can be explained by lowering resistivity of the composite derived from the ferrite conductivity, which starts to dominate in the range of high concentrations of the ferrite phase. The reduced resistivity makes impossible sufficient poling of ceramics.

Therefore, a high ME output might be obtained by a compromise to ensure: (a) a high ferrite concentration for a high magnetostrictively induced strain, (b) a good control of the microstructure, thus avoiding the formation of the conductive ferrite chains, favored at high ferrite concentrations.

1.2.Barium Titanate

1.2.1. Crystal Structure

Barium titanate ($BaTiO_3$) crystallizes in a perovskite structure which is characteristic of many compounds with a general chemical formula ABX_3, where A and B are cations, and X is an anion[26]. The perovskite structure consists of corner-linked BX_6 octahedrons (Fig. 3a)

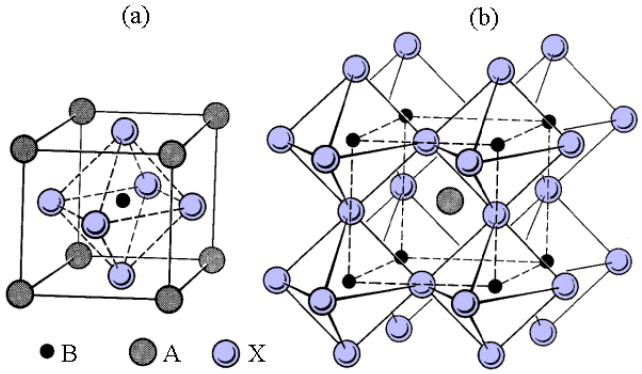

Fig 3. *Perovskite-type crystal structure. (a) Unit cell; (b) the structural framework consisting of octahedral (right)*

The octahedrons are connected in such a way that the linear octahedron chains which are parallel to each other can be identified on all three mutually perpendicular axes (Fig. 3b). The cations are located in the spaces between the octahedrons. Thus, if the B cations are surrounded by six X anions, then the A ions, which occupy the center of the cubic octahedron, are surrounded by 12 anions.

Above the Curie temperature (120°C) barium titanate has a cubic structure which belongs to the space group P*m*3*m* (Fig. 4a). The lattice constant is about 4 $\mathring{A}$. Below 120°C it becomes a ferroelectric tetragonal compound with the space group P4*mm* (Fig. 4b). At 20°C it has a = 3.992 $\mathring{A}$ and c = 4.036 $\mathring{A}$. The spontaneous polarization is in the direction of the c – axis along which the ions are displaced.

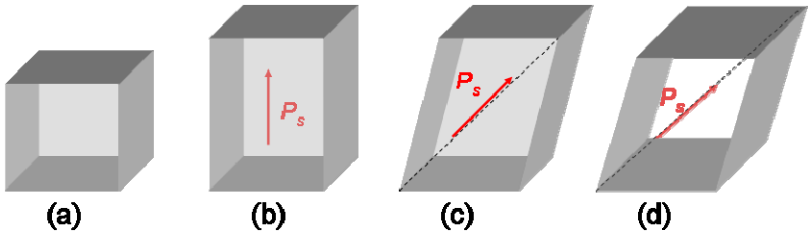

Fig 4. *The unit cell of $BaTiO_3$ in different phases. (a) Cubic cell; (b) tetragonal cell; (c) orthorhombic cell; (d) rhombohedral cell. The dashed lines represent initial cubic cell. The arrow indicated the direction of spontaneous polarization.*

A phase transition from a tetragonal phase to a ferroelectric orthorhombic phase occurs near 0°C (Fig. 4c). The spontaneous polarization occurs diagonally to the face of the cubic unit cell, and the lattice is lengthened in the same direction. As a result, a cell acquires a monoclinic distortion. The symmetry is described by the space group C2*mm*. At –10°C we have a = 5.682 Å , b = 5.669 Å , and c = 3.990 Å .

A transition to the rhombohedral ferroelectric phase occurs in the in the temperature range of –90°C to –70°C (the space group *R*3*m*). In this phase the spontaneous polarization and cell elongation occur in the direction of the body diagonal of the cubic cell (Fig. 4d).

1.2.2. Dielectric properties

Above the Curie temperature, barium titanate is a cubic crystal and, therefore, is isotropic. The value of the dielectric constant, therefore, is the same in any crystallographic direction. Below the ferroelectric transition temperature, the anisotropic tetragonal phase is formed, which leads to different values of the dielectric constant measured in different crystallographic directions.

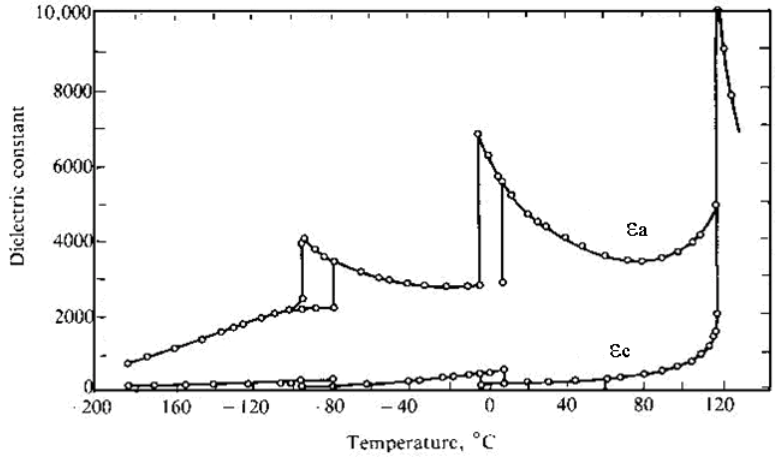

Fig 5. *Temperature dependence of the dielectric constant of barium titanate single crystal*

Fig. 5 is a plot of the dielectric constant vs. temperature measured for the two crystallographic directions of the tetragonal phase. The domain structure becomes more complex upon transition to the orthorhombic phase, and these curves no longer correspond to definite crystallographic directions.

1.2.3. Ferroelectric domains

Barium titanate, which is a cubic crystal above the Curie temperature, becomes a tetragonal crystal as the result of transition to the ferroelectric phase, so that its polar axis coincides with the tetragonal *c* – axis. Since any of the three mutually perpendicular fourfold axes of the cubic phase can be the *c* – axis, the spontaneous polarization should have six possible directions. Thus the angle between the polarization vectors of the domains can be equal to either 90° or 180°. The domains with a mutually perpendicular direction of the spontaneous polarization would form the 90° domain walls. Accordingly, the domains with the angles between the polarization vectors equal to 180° would form 180° domain walls. The allowed 90° domain walls, which are crystallographically preferred, coincide with the tetragonal {101} planes. Since the nonferroelectric phase has a center of inversion and the tetragonal deformation is independent of the direction of the spontaneous polarization, the 180° domain wall belongs to the arbitrarily oriented, allowed domain walls.

Typical ferroelectric domain structure of barium titanate single crystal (or epitaxial thin film) is given in Fig. 6[27]

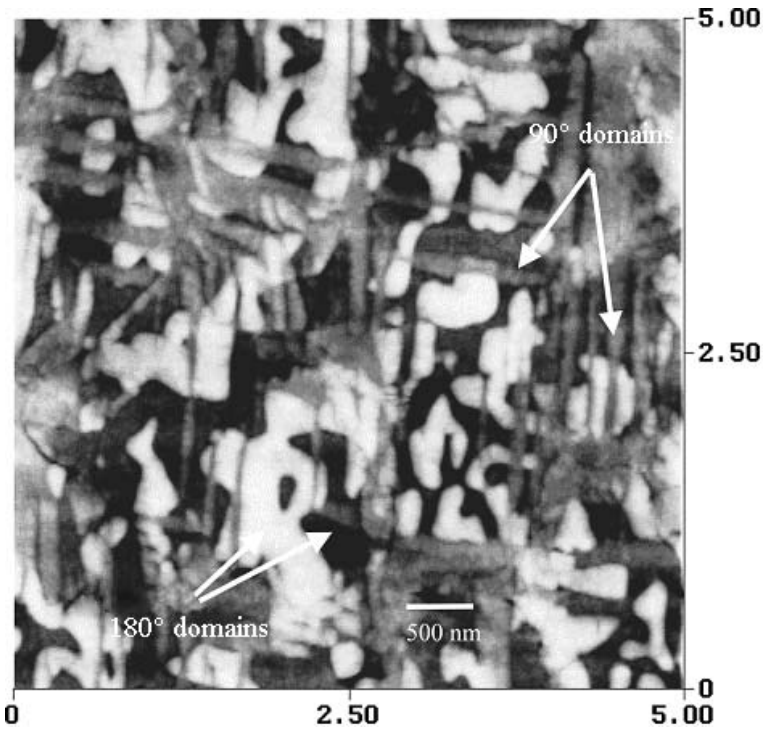

Fig 6. *Barium titanate ferroelectric domain structure*

1.3.Hexagonal ferrites

Hexagonal ferrites are a numerous family of related compounds with hexagonal and rhombohedral symmetry. All of them are synthetic except magnetoplumbite, of approximate formula $PbFe_{7.5}Mn_{3.5}Al_{0.5}Ti_{0.5}O_{19}$, which is the only natural component isomorphous with barium ferrite, $BaFe_{12}O_{19}$[28].

The composition of the various compounds can be understood by examining the upper section of the ternary phase diagram $MeO – Fe_2O_3 – BaO$, where Me is a divalent metal such as Ni, Mg, Co, Fe, Zn, Mn or Cu, (Fig. 7). All the ferrites are found on the joins $BaFe_{12}O_{19} – Me_2Fe_4O_8$ and $BaFe_{12}O_{19} – Me_2BaFe_{12}O_{22}$, or M – S and M – Y, respectively. M, S, and Y are the end-members.

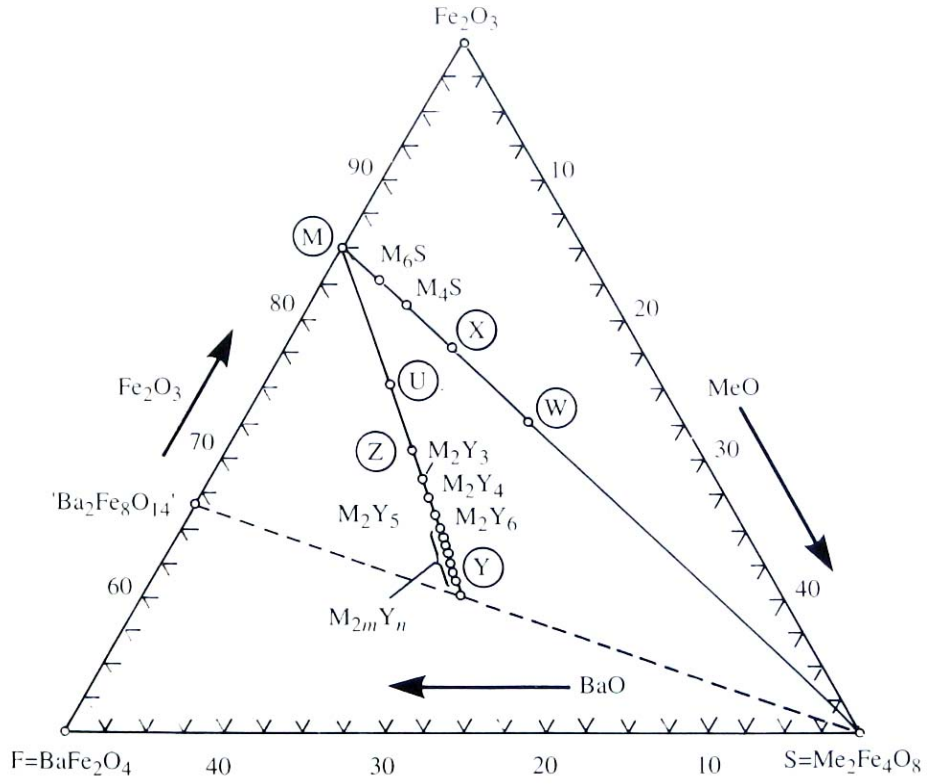

Fig 7. *The upper triangle of the ternary phase diagram $MeO – Fe_2O_3 – BaO$*

1.3.1. M-ferrites

1.3.1.1. Crystal and Magnetic structure

The compounds $BaFe_{12}O_{19}$ and $SrFe_{12}O_{19}$ are the most important hexagonal ferrites, and are used on a very large scale as permanent magnets[29]. The crystal structure, known as the magnetoplumbite structure, is shown in Fig. 8

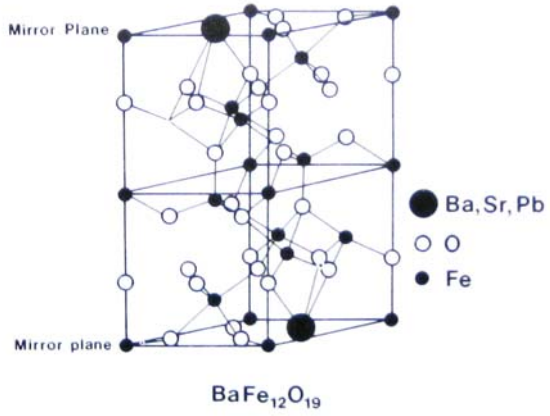

Fig 8. *Rhombohedral cell of hexagonal unit cell of $BeFe_{12}O_{19}$ or $SrFe_{12}O_{19}$*

The unit cell contains two formula units, and can be divided into four blocks, designated as SRS*R*, arranged as shown in Fig. 9. The asterisk signifies that the block has been rotated by 180° about the *c*-axis. The S blocks have the spinel structure, but are oriented so that the [111] direction is parallel to the c-axis. Since the R-blocks have a rhombohedral structure, the overall symmetry of the unit cell is rhombohedral (since this has a lower symmetry), with a = 0.588 nm and c = 2.32 nm.

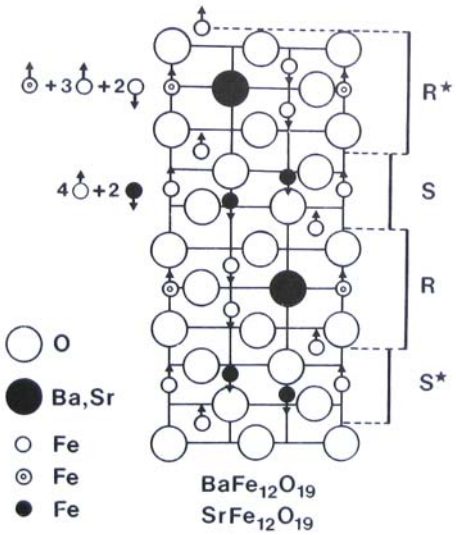

Fig 9. *Projection of the unit cell of barium or strontium ferrite, showing that it can be divided into four blocks designated as R*SRS**

This rhombohedral unit cell has one third of the volume of the hexagonal unit cell and has the same symmetry. The relationship between the two unit cells is shown in Fig. 10. For crystallographic studies it is usually more convenient to use the smaller rhombohedral cell, though $BaFe_{12}O_{19}$ and $SrFe_{12}O_{19}$ and similar material are often referred to as the hexagonal ferrites.

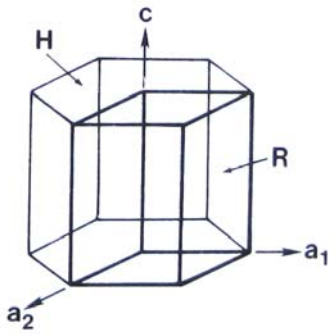

Fig 10. *Relationship between rhombohedral (R) and hexagonal (H) unit cells in $BaFe_{12}O_{19}$ or $SrFe_{12}O_{19}$*

The ferrimagnetism is produced entirely by the 24 Fe^{3+} ions, each of which has a magnetic moment of 5 μ_B. These ions occupy three kinds of crystallographic sites: tetrahedral, octahedral and fivefold coordination sites. The directions of the individual magnetic moments are shown in Fig 9.

One of the most important properties of $BaFe_{12}O_{19}$ (and $SrFe_{12}O_{19}$) is very high uniaxial magnetocrystalline anisotropy. The easy directions of magnetization are of course parallel and antiparallel to the hexagonal *c*-axis, so that a single crystal can be easily saturated along this axis.

1.3.1.2. Permanent magnet properties

The permanent magnet properties of $BaFe_{12}O_{19}$ were discovered by Went *et al.*[30], who showed that when fine particles of the material with diameters of order 1 μm are sintered into a solid compact of high density, it is possible to obtain intrinsic coercivities of about 380 kA m^{-1} in combination with a remanent magnetization of about 0.2 T. Barium ferrite magnets are usually prepared as follows. Fine powders of $BaCO_3$ and Fe_2O_3 are first carefully mixed in the ratio 1:6; then they are calcined in a furnace at about 1200°C, after which the resulting material $BaFe_{12}O_{19}$ is ground to a fine powder with a particle size of order 1 μm. This material is then pressed with or without a magnetic field and sintered at 1200°C in an oxidizing atmosphere. After the calcination process platelets of the hexagonal $BaFe_{12}O_{19}$ are formed in which the easy direction of magnetization is perpendicular to the plane of the platelets but parallel to the easy hexagonal axis of magnetization as shown in Fig. 11. This fortuitous growth habit is very advantageous, since during the pressing process, the planes of the hexagonal platelets tend to lie parallel to each other so as to minimize the total volume of the compact in the most energetically favorable way. However, since the preferred axis of magnetization due to the magnetocrystalline anisotropy is

parallel to a hard direction due to the shape anisotropy, the demagnetizing field due to the latter assist the magnetization reversal process.

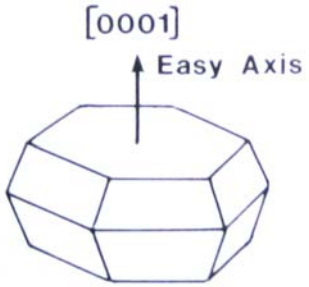

Fig 11. *Hexagonal crystal platelet of $BaFe_{12}O_{19}$ or $SrFe_{12}O_{19}$ with the arrow indicating the easy axis of magnetization*

Strontium ferrite $SrFe_{12}O_{19}$ is almost identical with $BaFe_{12}O_{19}$ in its crystallographic structure and magnetic properties, except that the sintered magnets generally have higher coercivity.

Barium and strontium ferrites can be heated in air to temperature well above the Curie temperature (about 450°C) without structural damage, and hence no irreversible loss of their permanent magnet properties, which reappear after cooling. Indeed, the structure remains stable up to about 1400°C in air before oxygen is released and phase transformations occur.

1.3.2. Z-ferrites

Z – ferrite belongs to the new class of planar hexagonal ferrites with the general chemical formula $Ba_3M_2Fe_{24}O_{41}$, which was discovered between 1952 and 1956 by Phillips (see, e.g. [32]. and references therein).The crystallographic structure is really complex. It consists of alternating basic units of hexagonal barium M and Y ferrites. The software simulation (Powdercell 2.4) of the unit cell structure is given in Fig. 12. Z – ferrites usually retain a hexagonal structure with the direction of magnetization parallel to the c – axis. For Co_2Z the easy axis is in the c – direction above 200°C, between – 50° and 200°C it lies in the basal plane and below – 50° on a cone making an angle with the c – axis[31]. As a consequence of this, at room temperature this material is magnetically soft because, although a large amount of energy is needed to move out of the basal plane, the magnetic vector can easily rotate within the preferred plane[32].

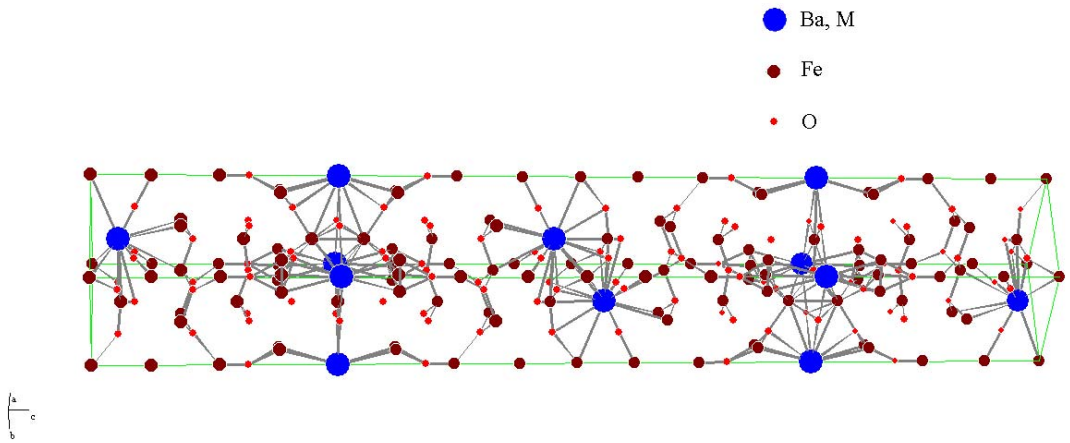

Fig 12. *Unit cell structure of Z –ferrite*

The main magnetic properties, such as unit cell parameters (a_0, c_0), molecular weight, coercive field (H_C), magnetization saturation (M_S) and the Curie temperature (Θ_C) of the M and Z – ferrites are summarized in Table. 1[31, 33, 34]

	c_0, Å	a_0, Å	Molecular weight, g/mol	H_C, mT	M_S, emu/g	Θ_C,°K
BaM	23,18	5, 889	1112	503.9	58.4	450
SrM	23,03	5,864	1062	552.9	65	460
Co_2Z	52,30	5,88	2526	6.72	48.62	410

Table 1. *Magnetic properties of the hexagonal M and Z compounds [Smit and Wijn, 1959; Von Aulock, 1965, and Braun, 1957]*

2. Motivation

The composites studied in present work were sintered for the first time by R. Pullar and present the initial results on the characterization of magnetoelectric composites based on $BaTiO_3$ and hexagonal ferrites: barium hexaferrite ($BaFe_{12}O_{19}$), strontium hexaferrite ($SrFe_{12}O_{19}$) and barium-cobalt Z-ferrite ($Ba_3Co_2Fe_{24}O_{41}$).

The first two basic matters one should consider while synthesizing a new composite are: 1) individual properties of the components, 2) sufficient connectivity between the components.

As it was discussed earlier, the individual properties of the components would contribute to so-called sum property. Therefore, the better are the properties of the components, the better properties one may expect from the composite. From this point of view, the choice of barium titanate as a ferroelectric phase component, as well the indicated ferrites as the magnetic phase component is reasonable. Barium and strontium hexaferrites are used on a very large scale as permanent magnets, cobalt Z – ferrites are known for their GHz range application, while barium titanate is simply a cornerstone of all ferroelectrics. They are chemically compatible and have similar melting temperatures.

However, in most cases it is not only the sum property one is interested in, but also the product property, a novel phenomena originated from the mutual interaction between the individual phases, such as magnetoelectric effect. To achieve that, good phase connectivity between the phases is really needed. Naturally, in this aspect, laminated composites may exhibit better properties. However, their fabrication is far more complicated, and might not be very efficient, since the unit cell of barium titanate and the used ferrites could be mated. Thus standard simple fabrication route should be first applied.

The studied systems are also attractive for pedagogical purposes. First, combining both ferroelectric and magnetic phases this system offers an access to a variety of measurement techniques which can be implemented in order to study the properties of both phases. This gives an opportunity not only to learn about the new techniques, but also to improve skills for already known methods. For instance, it gives the best opportunity to operate the atomic force microscope, since ferroelectric and magnetic domain imaging involve totally different operation modes, namely piezoresponse and magnetic force microscopy. Second, being a new system, it is still made of very well known and studied building blocks, like barium titanate and hexagonal ferrites. There is lots of information available either in the textbooks, allowing deeper understanding of the nature of all the phenomena, and in the articles, which give the directions of present investigations and allows comparison of the obtained results with the previous ones reported by others.

3. Experimental

3.1. Sample preparation

The samples studied in present work were synthesized by Dr. R. C. Pullar, Department of Materials, Imperial College (London, UK).

Though M-hexaferrite systems were first synthesized in 1946, a lot of results have been reported on a coexistence of metastable phases, such as $\alpha - Fe_2O_3$ within M-ferrites. In order to achieve the pure $BaFe_{12}O_{19}$ or $SrFe_{12}O_{19}$ structure, a very precise compositional range should be used. Many authors reported on the nonstoichiometric mixing of the precursors. For instance, in the case of barium hexaferrite, an iron – deficient mixture with Fe/Ba ratio of 10 to exactly 12 is sometimes needed to form a single phase product[35]. For $SrFe_{12}O_{19}$ the M-phase forms as a pure product in a nonstoichiometric mixture with an Fe/Sr ratio of 9.23[36]. However, R. C. Pullar have been adding a stoichimetric amount of barium and strontium precursors while synthesizing a single phase M-ferrites[33, 37, 38].

The typical method to obtain M-hexaferrite compounds is the solid state reaction. This method consists of heating the mixtures of relevant oxides at temperatures as high as 1000°C. However, Benito *et al.*[39] reported that the reduction of the particle size leads to an increase in the specific surface area, which in turn facilitates the diffusion process, one of the main mechanisms of the formation of barium ferrite particles. This results in formation of barium hexaferrite at lower temperatures. Among the other methods that have been reported, there are chemical co-precipitation[40], sol-gel[33, 37, 38, 41], mechanical alloying[42] etc.

Synthesis of Z-ferrite systems is more complex. As it was first reported by M. A. Vinnik in 1965 the Z phase can be considered as an alternated stacking of two other hexagonal ferrite phases, BaM ($BaFe_{12}O_{19}$) and Co_2Y ($Ba_2Co_2Fe_{12}O_{22}$), and although the formation process is still not fully understood it seems that the M and Y phases must coexist first before the Z phase can crystallize, probably through topotactic reaction[43]. High calcination temperatures (1100 – 1400°C) are usually required for the solid reaction to occur. Still, conventional ceramic process (one-step calcination) often results in Z-phase coexisting with one or both of the phases M, Y. The results reported by J. Jeong *et al*[44] showed that pure Z-phase can be obtained by two-step calcination technique, namely, either of the two ways: precalcination at 900°C and postcalcination at 1350°C or precalcination at 1100°C and postcalcination at 1350°C. A completely different synthesis route resulting in formation of the pure Z-ferrite phase was proposed by G. Xiong *et al.*[45]. They used the steric acid sol-gel method with reaction temperatures starting from 750°C.

In the present study the three ferrite powders, $BaFe_{12}O_{19}$, $SrFe_{12}O_{19}$ and $Ba_3Co_2Fe_{24}O_{41}$ where synthesized from stoichiometric mixtures of $BaCO_3$, Fe_2O_3, SrO and Co_3O_4, and calcined at 1150, 1100 and 1250^oC respectively.

$BaTiO_3$ was the commercial powder from AlfaAesar, (99+%, 0.05-0.07 μm particle size)

Following this, each of the prepared ferrite powders was dry mixed with barium titanate powder on a ball mill without solvent for 24 hours, then pressed as pellets Ø13 mm x 4 mm or Ø8mm x 2 mm in a uniaxial press, pressure of 0.25 Torr, and then sintered in air at 1250 °C for 2 hours with heating and cooling rates of 5 °C /min.

3.2.Characterization

3.2.1. Structural analysis

3.2.1.1. X-ray powder diffraction (XRD) measurement

Powder diffraction (XRD) is a technique used to characterize the crystallographic structure, grain size, and preferred orientation in polycrystalline or powdered solid samples. Powder diffraction is commonly used to identify unknown substances, by comparing diffraction data against a database maintained by the International Centre for Diffraction Data. It may also be used to characterize heterogeneous solid mixtures to determine relative abundance of crystalline compounds and, when coupled with lattice refinement techniques, such as Rietveld refinement, can provide structural information on unknown materials.

Figure 13. shows the basic features of an XRD experiment, where the diffraction angle 2θ is the angle between the incident and diffracted X-rays. In a typical experiment, the diffracted intensity is measured as a function of 2θ and the orientation of the specimen, which yields the diffraction pattern. The X-ray wavelength λ is typically 0.7 – 2Å, which corresponds to X-ray energies of 6 – 17 keV[46].

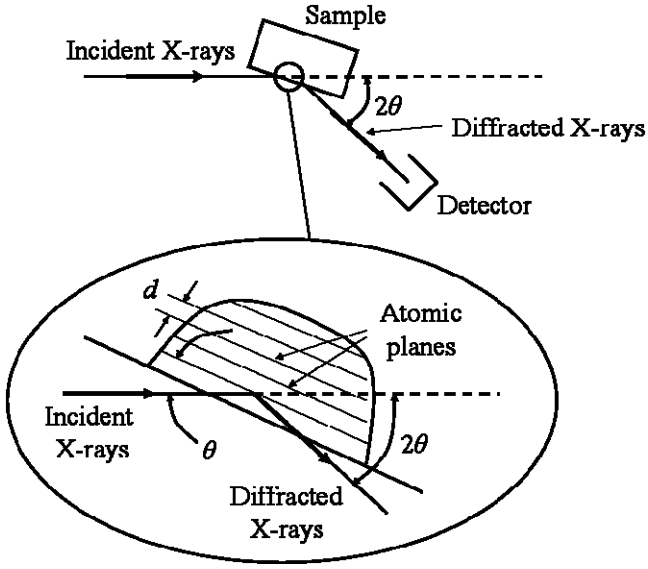

Fig 13. *Basic features of an XRD experiment*

Crystals consist of planes of atoms that are spaced at a distance d, but can be resolved into many atomic planes, each with a different d-spacing.

When there is a constructive interference from X-rays scattered by the atomic planes in a crystal, a diffraction peak is observed. The condition for constructive interference from planes with spacing d is given by Bragg's law:

$$\lambda = 2d \sin\theta \tag{2}$$

where θ is the angle between the atomic planes and the incident (and diffracted) X-ray beam (Fig. 11). For diffraction to be observed, the detector must be positioned so as the diffraction angle is 2θ, and the crystal must be oriented so that the normal to the diffracting plane is coplanar with the incident and diffracted X-rays and so that the angle between the diffracting plane and the incident X-rays is equal to the Bragg angle θ.

The X-ray diffraction of powder samples results in a pattern characterized by peaks in intensity at certain positions. The height, width and position of these peaks can be used to determine many aspects of the materials structure. The Rietveld method uses a least squares approach to refine a theoretical line profile until it matches the measured profile.

The peak shape is assumed almost exactly matching Gaussian distribution. This allows calculation a contribution of a given peak to the profile y_i at the position $2\theta_i$:

$$y_i = I_k \exp\left[-4\ln\left(\frac{2}{H_k^2}\right)(2\theta_i - 2\theta_k)^2\right] \tag{3}$$

where H_k is the full width at half peak height (full-width half-maximum), $2\theta_k$ is the centre of the peak, and I_k is the calculated intensity of the peak.

At very low diffraction angles the peaks may acquire an asymmetry due to the vertical divergence of the beam. Rietveld used a semi-empirical correction factor, A_s to account for this asymmetry:

$$A_s = 1 - \left[\frac{sP(2\theta_i - 2\theta_k)^2}{\tan\theta_k} \right] \quad (4)$$

where P is the asymmetry factor and s is +1, 0, -1 depending on the difference $2\theta_i - 2\theta_k$ being positive, zero or negative, respectively.

At a given position more than one diffraction peak may contribute to the profile. The intensity is simply the sum of all peaks contributing at the point $2\theta_i$.

The width of the diffraction peaks is found to broaden at higher diffraction angles. This angular dependency was originally represented as

$$H_k^2 = U\tan^2\theta_k + V\tan\theta_k + W \quad (5)$$

where U, V and W are the halfwidth parameters and may be refined during the fit.

The principle of the Rietveld method is to minimize the function M which represents the difference between the calculated profile *y(calc)* and the observed data *y(obs)*. Rietveld defined such an equation as:

$$M = \sum_i W_i \left\{ y_i^{obs} - \frac{1}{c} y_i^{calc} \right\}^2 \quad (6)$$

where W_i is the statistical weight and c is an overall scale factor such that $y^{calc} = cy^{obs}$

The quality of the agreement between observed and calculated profiles is measured by a set of nowadays-conventional factors[47], such as:

- Profile factor R_p, to be minimized in the least-squares fitting process,
- Weighted profile factor R_{wp}, that is used to emphasize intense peaks over background,

- Expected weighted profile factor R_{exp} that is used to estimate the best value R_p for a data set. It is an evaluation how good the data are.
- The goodness of fit $\chi^2 = (R_{wp}/R_{exp})^2$

X-ray powder diffraction patterns of the samples were recorded in the region of 2Θ = 10 – 80° with a scanning speed of 0.25°/min on a Philips PW1710 diffractometer using Cu K_α radiation with a nickel filter.

The first analysis of the XRD data was performed with Rietveld program Powdercell 2.4. This software allows not only fitting the XRD profile of the database to the observed curve, but it also simulates the crystallographic structure of the analyzing compound. The last feature is especially useful for the beginner. It allows not only visualization of the unit cell at any angle, but also it develops an additional interest for the software and the technique itself.

However, in present case, most of the spectra have a very high level of background noise. This greatly affected the quality of the fitting. The R_{wp} parameter in most cases was over 20, while for the reliable fitting it should be around 10.

Therefore, as the second attempt to improve the situation, Rietica 1.7.7 package was used. This software is similar to Powdercell, since it also utilizes Rietveld method, although it has an additional feature which was found to be very useful in the given case. Rietica includes the additional parameters for fitting the background. Counting on this, the following sequence of steps was taken:

1) Fitting the background by allowing variation of polynomial coefficients (*A-1*, *A0*, *A1*, *A2*, *A3*, *A4*) corresponding to approximated background curve.
2) Fitting the shape of the spectra by allowing variation of *U*, *V*, *W* parameters (the parameters of the background curve polynomial are in the fixed position)
3) Fitting the position of the diffraction peaks by allowing variation of the unit cell parameters, *a* and *c* (all previously approximated parameters are in fixed position). Keeping in mind the Bragg's law, one could see that increase in a unit cell parameter would lead to the shift of the peak corresponding to the plane consisting the changing side of the cell to the left (towards the decreasing angle values)
4) Repeating steps 1 – 3 in order to check if the fitting is the best possible. Normally all the fitted parameters wouldn't change much from the previous values.

As the result, the agreement quality factor χ^2 in all of the spectra never exceeded 4 – the upper limit to consider the obtained data reliable. The values of χ^2 are listed in Table 2

Fig. 14 represents diffraction data of the pure ferrites (a – c) and barium titanate (d) together with the curves of the international database after the fitting procedure:

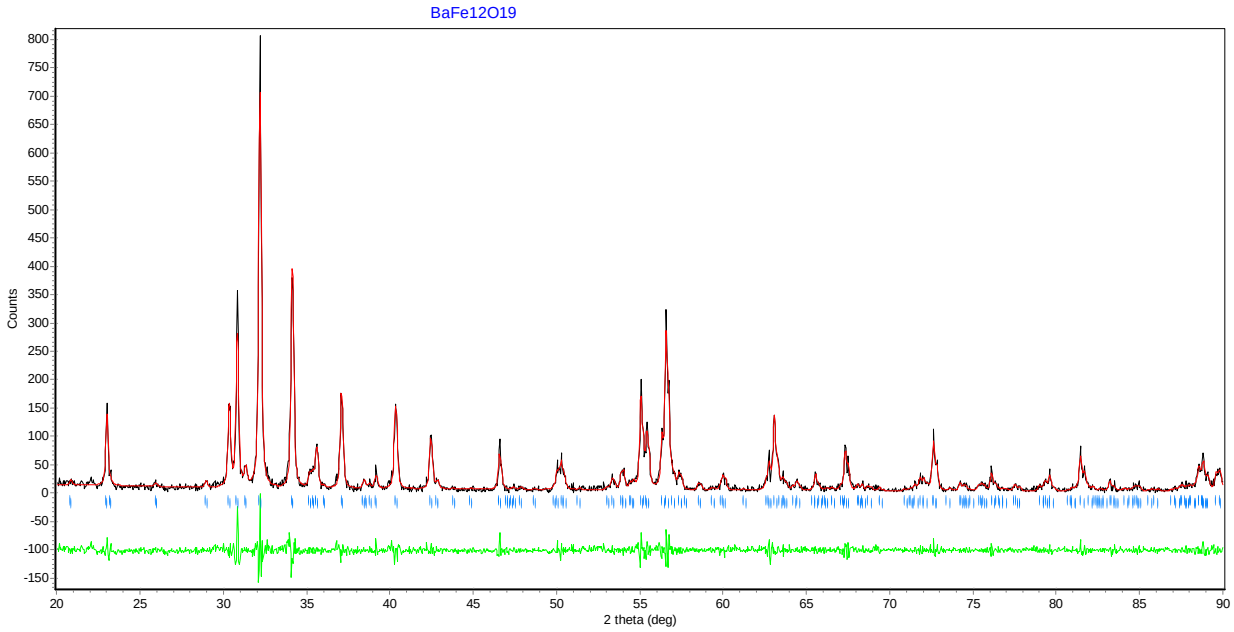

(a)

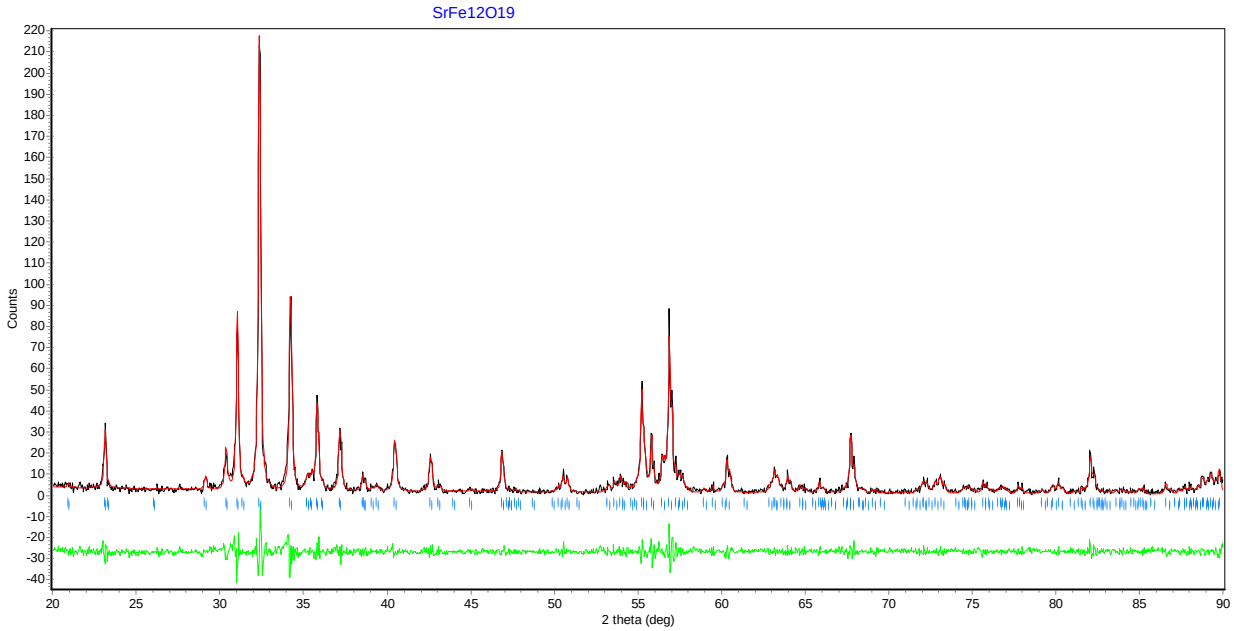

(b)

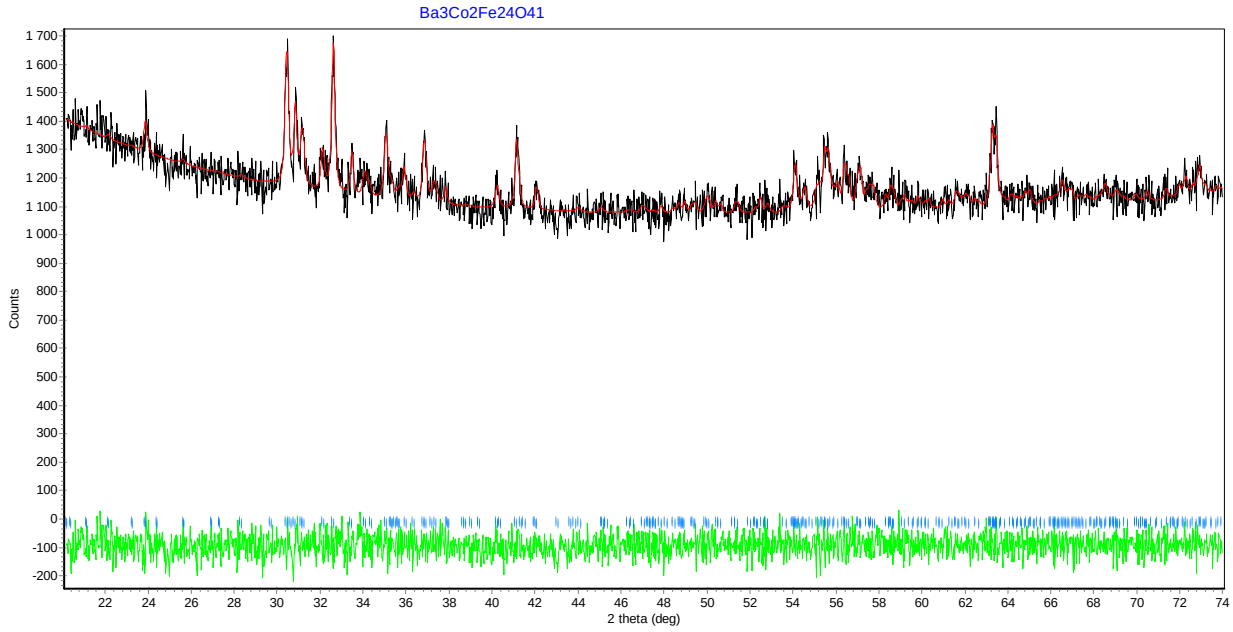

(c)

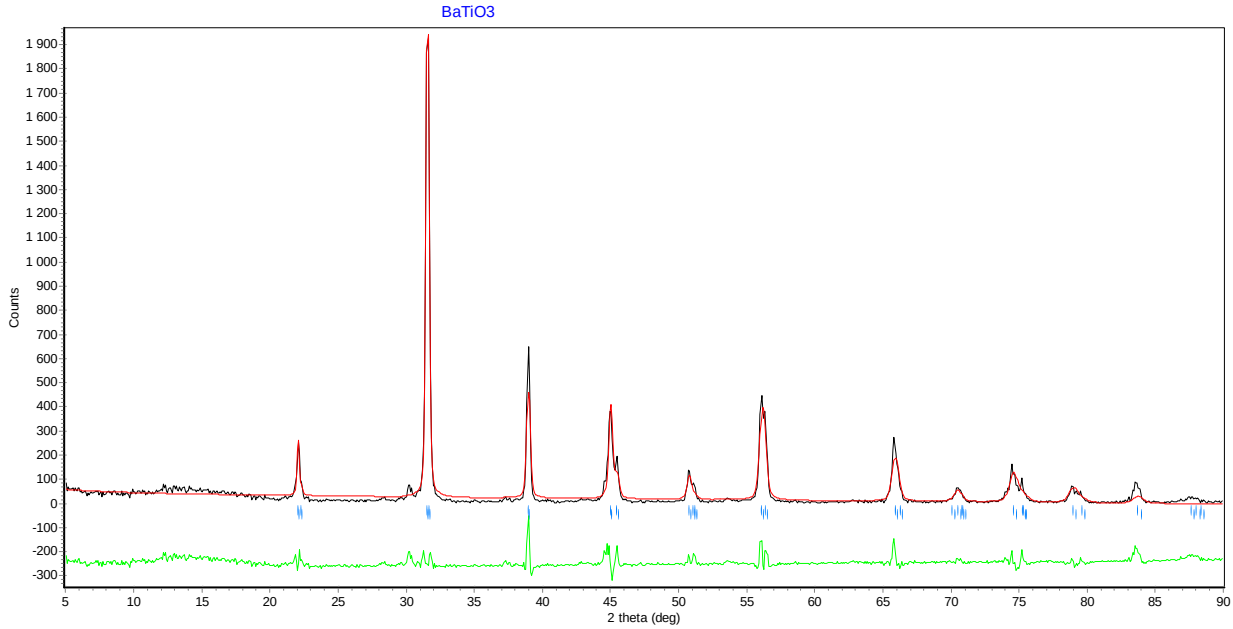

(d)

Fig 14. *XRD data of the pure ferrites (a) $BaFe_{12}O_{19}$, (b) $SrFe_{12}O_{19}$, (c) $Ba_3Co_2Fe_{24}O_{41}$ and (d)$BaTiO_3$. The green curve is the difference between the experimental data and the values of the database*

The XRD analysis of the composites was performed for all the compositions. However, due to a very small fraction of magnetic phase in the samples containing 10% of the ferrites, the intensity of the corresponding peaks was very low. This didn't allow analysis of these compositions by means of XRD technique. Therefore, the plots presented below (Fig. 15), as

well as further analysis of the XRD data correspond only to the compositions containing 50% of the magnetic phase.

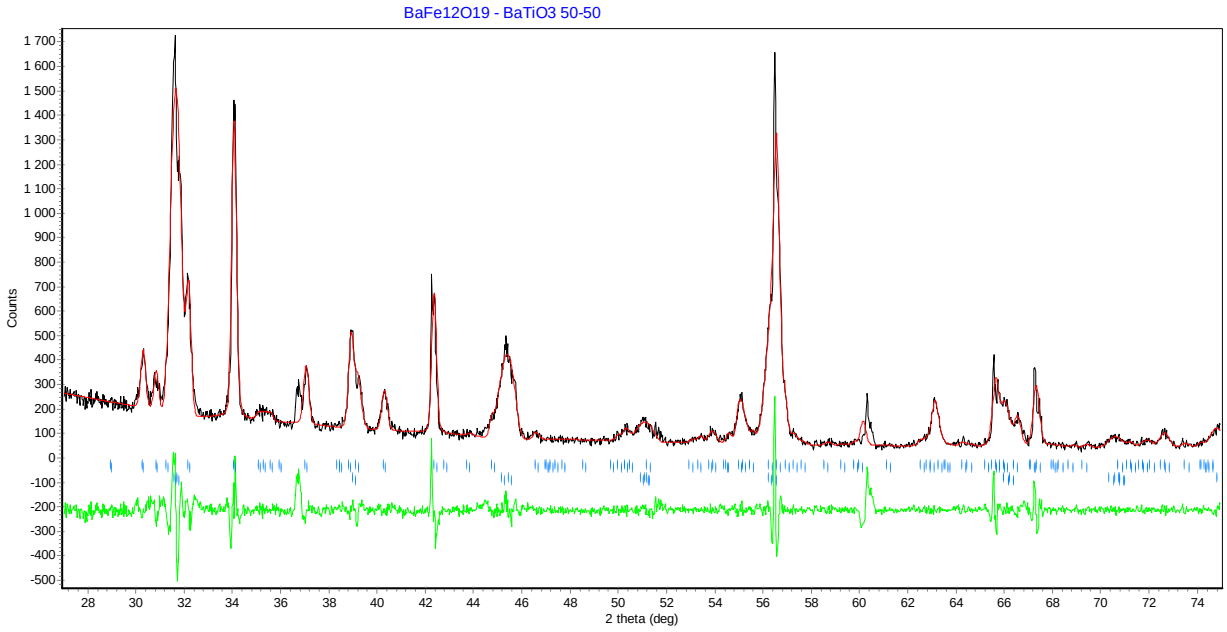

(a)

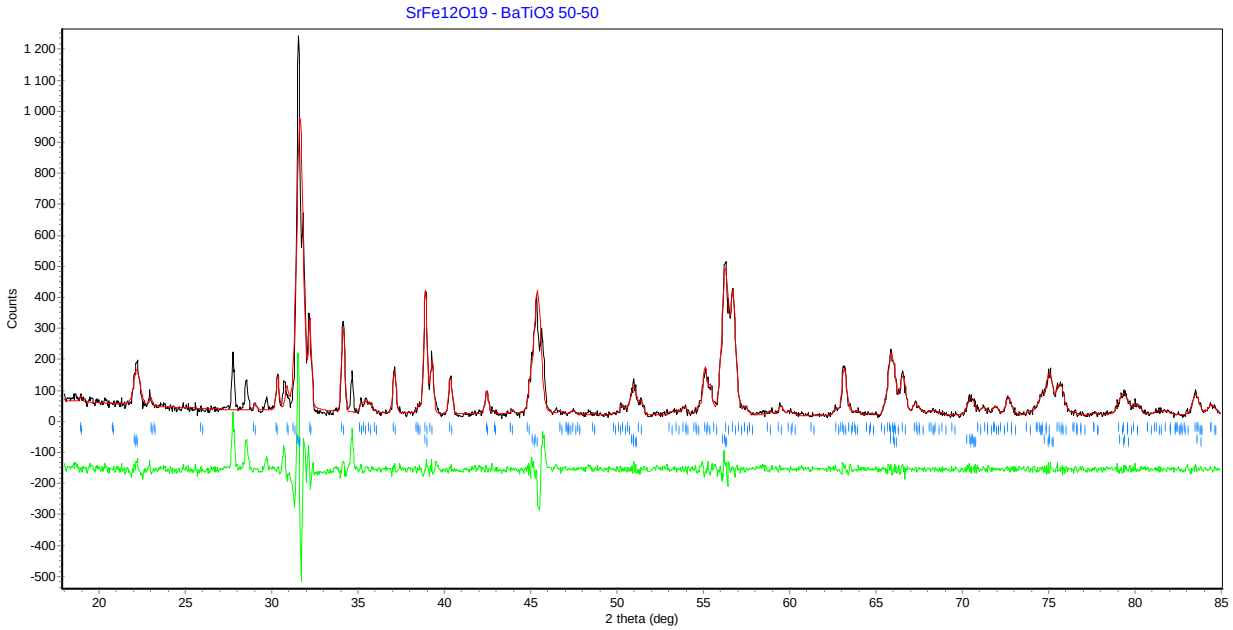

(b)

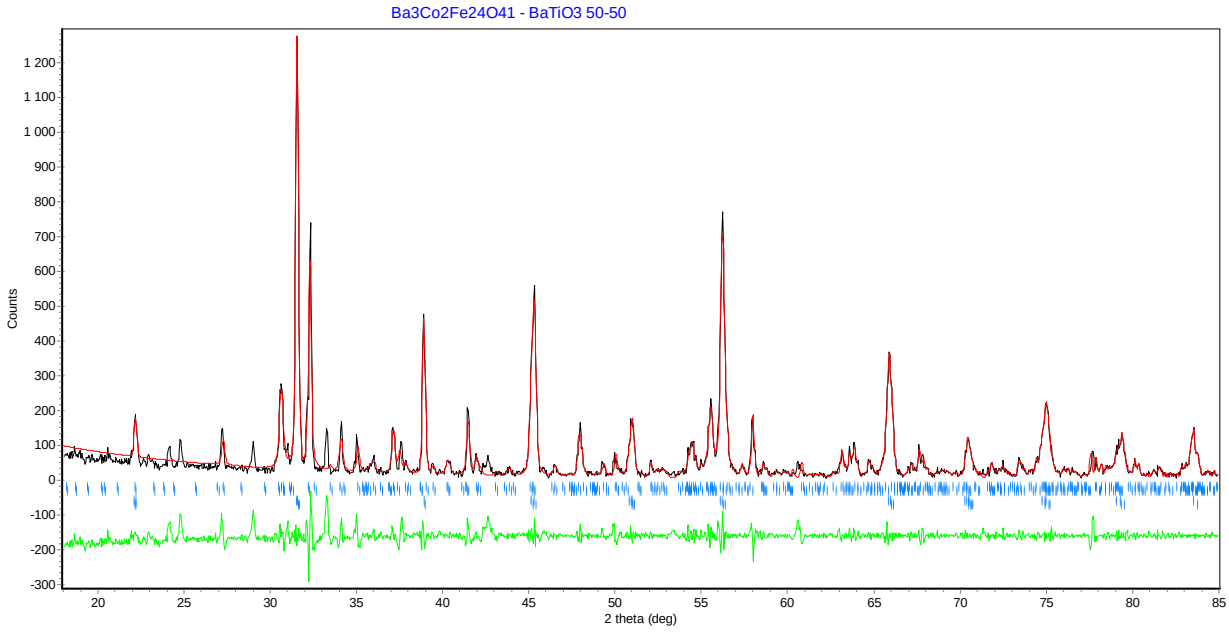

(c)

Fig 15. *XRD data of the composites (a) $BaFe_{12}O_{19}$ 50% – $BaTiO_3$ 50%, (b) $SrFe_{12}O_{19}$ 50% – $BaTiO_3$ 50%, (c) $Ba_3Co_2Fe_{24}O_{41}$ 50% – $BaTiO_3$ 50%. The green curve is the difference between the experimental data and the values of the database*

The changes in the unit cell dimensions compared to the corresponding structure were analyzed. The results are summarized in Table 2.

		a, Å	c, Å	a/c	V, Å^3	χ^2
$BaFe_{12}O_{19}$	ICSD (16157)	5.89280	23.2010	3.93716	2093.16	-
	100%	5.88970	23.1955	3.93856	2095.65	1.423
	50%	5.90130	23.1752	3.92727	2096.87	3.234
$SrFe_{12}O_{19}$	ICSD (66403)	5.88210	23.0230	3.91405	2069.57	-
	100%	5.88100	23.0333	3.91650	2069.72	0.345
	50%	5.88333	23.0806	3.92311	2075.59	3.177
$Ba_3Co_2Fe_{24}O_{41}$	ICSD (97980)	5.87740	52.2590	8.89126	4690.12	-
	100%	5.87730	52.2425	8.88888	4688.48	1.476
	50%	5.85760	52.2593	8.92140	4658.60	2.924
$BaTiO_3$	ICSD (15453)	3.99450	4.01335	1.00472	64.0371	-
	100%	3.98490	4.02300	1.00956	63.8829	0.390
	+ $BaFe_{12}O_{19}$	3.99404	4.01180	1.00560	63.8010	3.234
	+ $SrFe_{12}O_{19}$	3.99460	4.00091	1.00363	63.9725	3.177
	+ $Ba_3Co_2Fe_{24}O_{41}$	4.00090	4.01330	1.00310	64.2417	2.294

Table 2. *Variation of lattice parameters in composites.*

3.2.1.2. Scanning electron microscopy (SEM)

Scanning electron microscopy (SEM) is a type of electron microscope that images the sample surface by scanning it with a high-energy beam of electrons in a raster scan pattern. The resolution of the SEM can approach a few nm and it can operate at magnifications that are easily adjusted from about 10x – 300,00x. Not only is topographical information produced in the SEM, but information concerning the composition near surface regions of the material is provided as well[46].

In SEM, a source of electrons is focused (in vacuum) into a fine probe that is rastered over the surface of the specimen (Fig. 16). As the electrons penetrate the surface, a number of interactions occur that can result in the emission of electrons or photons from the surface. A reasonable fraction of the electrons emitted can be collected by appropriate detectors, and the output can be used to modulate the brightness of a cathode ray tube (CRT) whose *x*- and *y*-inputs are driven in synchronism with the *x* – *y* voltages rastering the electron beam. In this way an image is produced on the CTR; every point that the beam strikes on the sample is mapped directly onto a corresponding point on the screen.

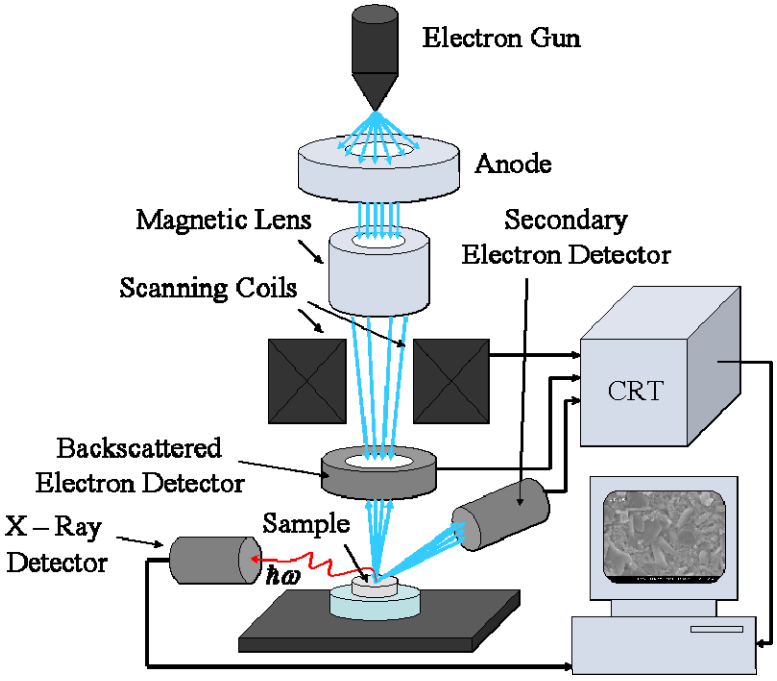

Fig 16. *Schematic describing the operation of SEM*

The principal images produced in SEM are of three types: secondary electron images, backscattered electron images, and elemental X – ray maps. Secondary and backscattered electrons are conventionally separated according to their energies. They are produced by

different mechanisms. Secondary electrons result from the inelastic scattering of electrons from the beam (primary electrons) with atomic electrons. During this process some energy is transferred to atomic electrons which allow the last to exit the solid. When the energy of the emitted electron is less than 50eV, by convention it is referred to as a secondary electron. Higher energy electrons are primary electrons that have been scattered without loss of kinetic energy (i.e., elastically) by the nucleus of an atom.

An additional electron interaction of major importance in the SEM occurs when the electron from the beam (primary electron) collides with and ejects a core electron from an atom in the solid. The excited atom will decay to its ground state by emitting a characteristic X – ray photon. The X – ray emission signal can be sorted by energy in energy dispersive X – ray detector. This forms the basis of the Energy Dispersive X-Ray Spectrometry (EDS), which is described below.

3.2.1.3. Energy Dispersive X-Ray Spectrometry (EDS)

Energy dispersive X-ray spectrometry (EDS) is an analytical technique used for the elemental analysis or chemical characterization of a sample. As a type of spectroscopy, it relies on the investigation of a sample through interactions between electromagnetic radiation and matter, analyzing X-rays emitted by the matter in response to being hit with charged particles. Its characterization capabilities are due in large part to the fundamental principle that each element has a unique atomic structure allowing X-rays that are characteristic of an element's atomic structure to be identified uniquely from each other. Most modern EDS systems can detect X-rays from all the elements in the periodic table above beryllium, Z = 4, if present in sufficient quantity.

X-rays are produced as a result of the ionization of an atom by high-energy radiation wherein an inner shell electron is removed[46]. To return the ionized atom to its ground state, an electron from a higher energy outer shell fills the vacant inner shell and, in the process, releases an amount of energy equal to the potential energy difference between the two shells. This excess energy, which is unique for every atomic transition, will be emitted by the atom as an X-ray photon. For example, if the K shell is ionized and the ejected K-shell electron is replaced by an electron from the L shell, the emitted X-ray is labeled a characteristic $K\alpha_1$ X-ray (Fig. 17). The hole that exists in the L shell will be filled by an electron from a higher shell, say the M shell, if one exists. This M – L transition may result in the emission of another X-ray, labeled in turn according to the one of the many M – L transitions possible. The cascade of transitions will

continue until the last shell is reached. Thus, in an atom with many shells, many emissions can result from a single primary ionization.

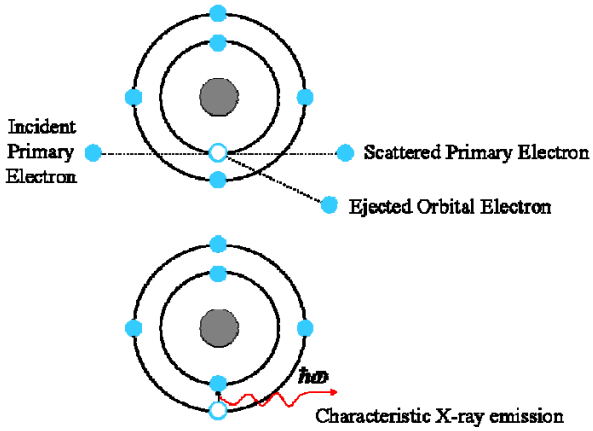

Fig 17. *Schematic of the inner shell ionization and subsequent de-excitation by X-ray emission*

The SEM images were taken for all the compositions. The magnifications were different for most of the samples and varied from 1000x to 6000x depending on the topographical features meant to be accentuated. The electron accelerating voltage was the same during all the experiments, namely 25 eV. Figs. 18 – 20 represent the results are supplemented with the EDS analysis of the units corresponding to the different phases. Owing to the difference in the unit cell structures (tetragonal for barium titanate, and hexagonal for the ferrites), the different phases are easily distinguished by the grain shape. The average grain size of the ferroelectric phase was found to be ~ 350 nm.

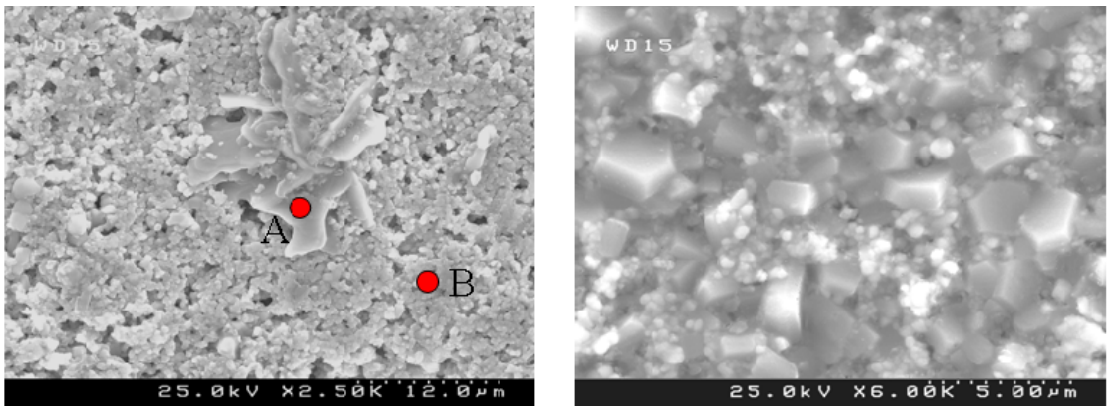

(a) (b)

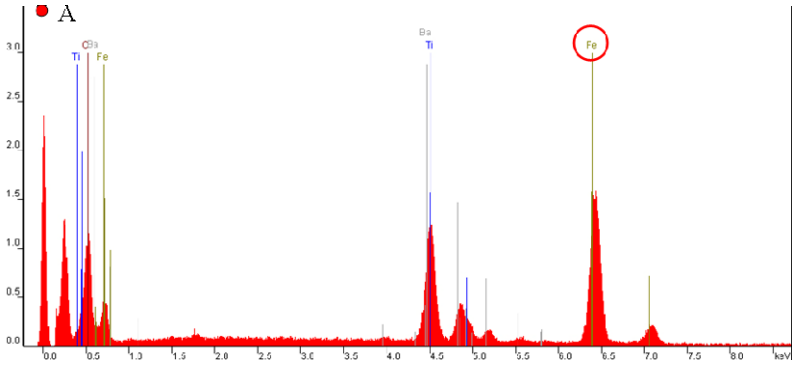

(c)

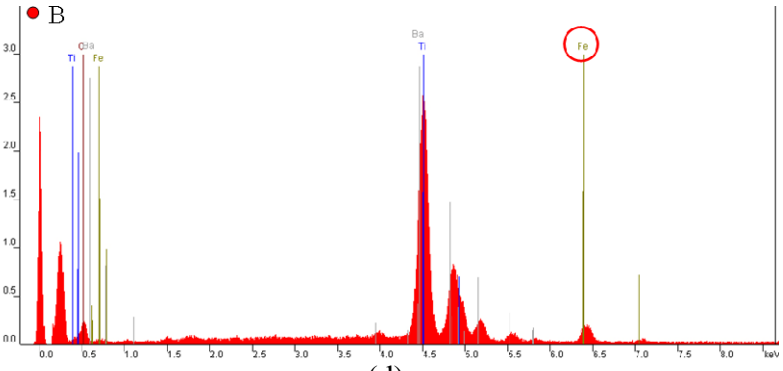

(d)

Fig 18. *SEM images of $BaFe_{12}O_{19} – BaTiO_3$ composites (a) 10% - 90%, (b) 50%-50%; EDS analysis of the corresponding phases (c) and (d)*

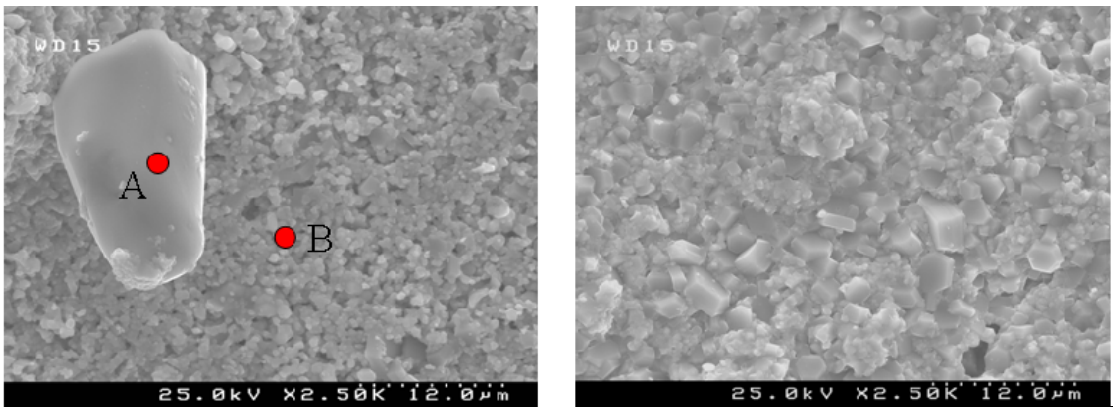

(a) (b)

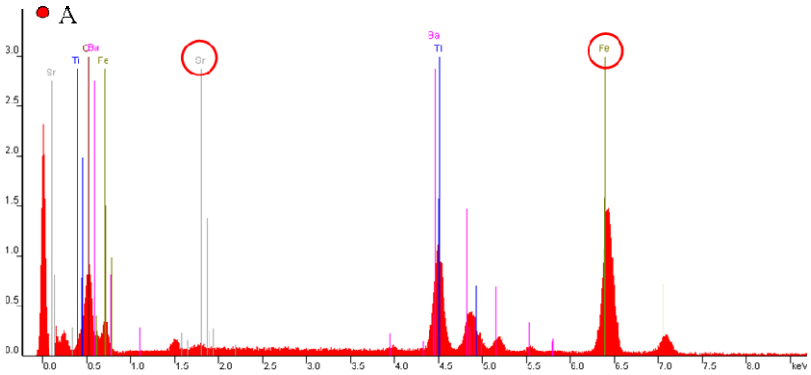

(c)

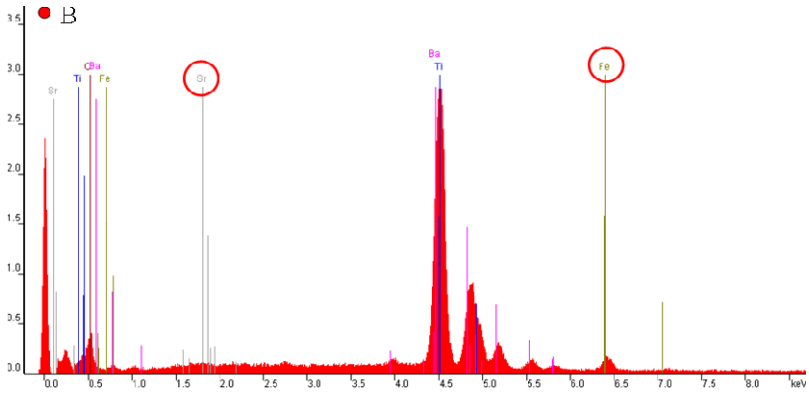

(d)

Fig 19. *SEM images of $SrFe_{12}O_{19} – BaTiO_3$ composites (a) 10% - 90%, (b) 50%-50%; EDS analysis of the corresponding phases (c) and (d)*

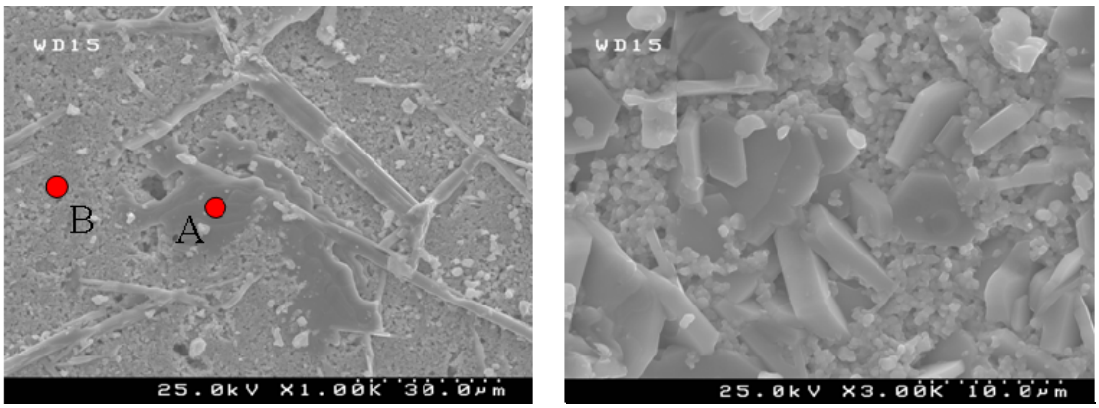

(a) (b)

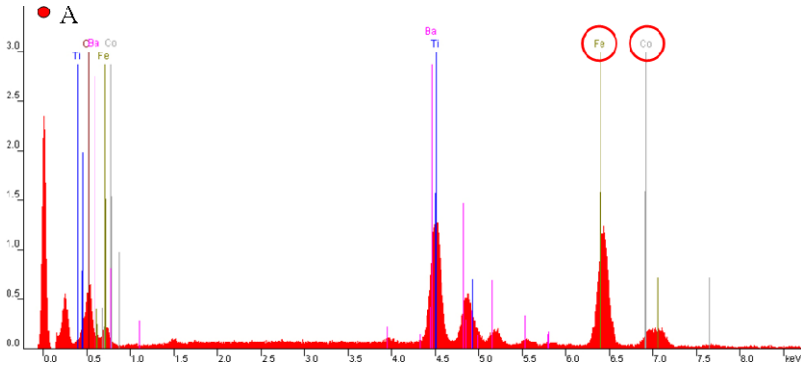

(c)

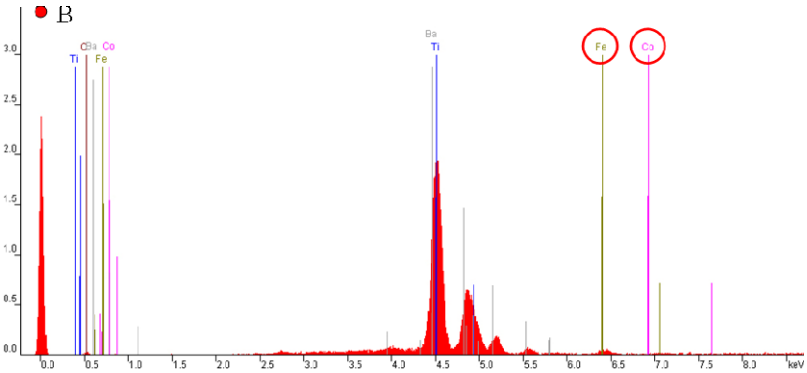

(d)

Fig 20. *SEM images of $Ba_3Co_2Fe_{24}O_{41}$ – $BaTiO_3$ composites (a) 10% - 90%, (b) 50%-50%; EDS analysis of the corresponding phases (c) and (d)*

3.2.2. Dielectric measurements

Capacitance and dissipation factor were measured in two modes: as a function of frequency in the range 1 Hz – 1 MHz at room temperature (for the composition $SrFe_{12}O_{19}$ 10% – $BaTiO_3$ 90%), and as a function of temperature at the fixed frequencies: 100 Hz, 1 kHz, 10 kHz, 100 kHz and 200 kHz for the compositions $BaFe_{12}O_{19}$ – $BaTiO_3$ and $SrFe_{12}O_{19}$ – $BaTiO_3$ with both fractions of the ferrite phase.

The measurements were performed with LCR meters E7-20 (working frequencies: 25 Hz – 999 Hz with step-interval 25 Hz, and 1 kHz – 1 MHz with step-interval 1 kHz) and MOTECH 4090D (fixed working frequencies: 100 Hz, 1 kHz, 10 kHz, 100 kHz and 200 kHz)

Since the studied samples were ceramics consisted of ferroelectric and non-ferroelectric phases, the effective dielectric permittivity was introduced.

The effective dielectric permittivity was converted from the measured values of capacitance by the following equation: $\varepsilon = kC\ [pF],\ k = 113\frac{d}{S}$, where d – sample's thickness (*mm*), and S – sample's area (mm^2). The geometry parameters of the samples and the conversion coefficient *k* are given in Table 3

	d, mm	*S,* mm^2	*k*
$BaFe_{12}O_{19}$ 10% - $BaTiO_3$ 90%	0.4	5	9.04
$BaFe_{12}O_{19}$ 50% - $BaTiO_3$ 50%	0.4	7	6.46
$SrFe_{12}O_{19}$ 10% - $BaTiO_3$ 90%	0.6	11	6.16
$SrFe_{12}O_{19}$ 50% - $BaTiO_3$ 50%	0.4	4.5	10.04

Table 3. *Geometry parameters of the sample and the conversion factor for the effective dielectric permittivity.*

Fig. 21 depicts frequency dependence of dielectric permittivity and dissipation factor for the composition $SrFe_{12}O_{19}$ 10% – $BaTiO_3$ 90%

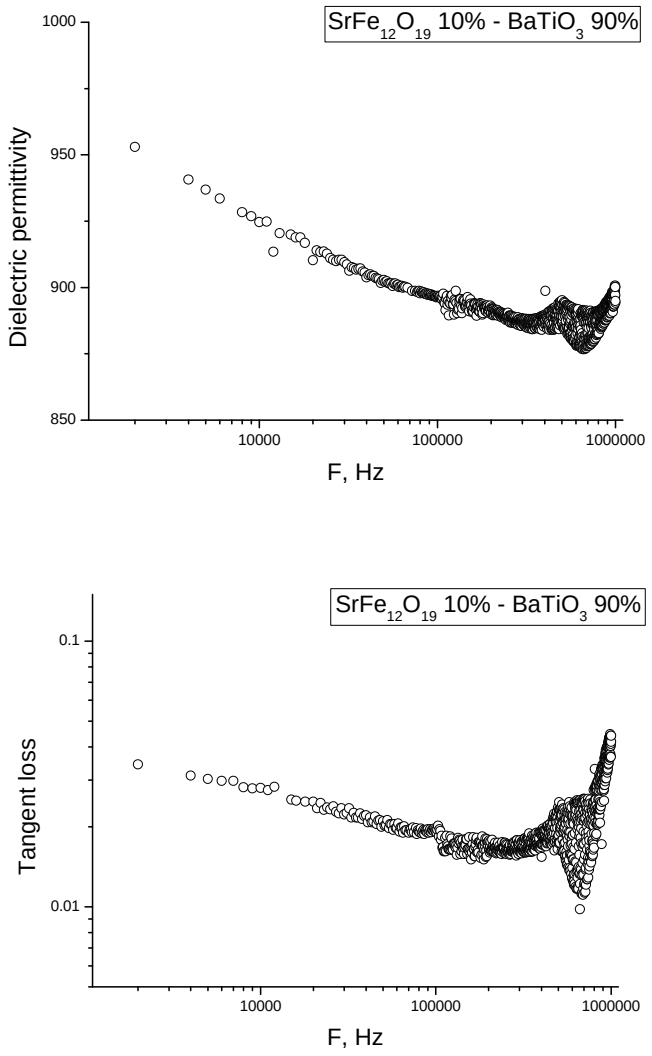

Fig 21. *Frequency dependence of dielectric permittivity and dissipation factor for $SrFe_{12}O_{19}$ 10% - $BaTiO_3$ 90%*

The temperature and frequency dependences of dielectric permittivity and dissipation factor for the compositions containing barium and strontium ferrites are given in Figs. 22 – 25. They show significant frequency relaxation (especially at high temperature) and broad dielectric peaks due to the phase transition in $BaTiO_3$. Unfortunately, high temperatures comprising ferromagnetic phase transitions in ferrite could not be assessed owing to the high conductivity of the samples even at high concentration of ferroelectric phase (90%). The experimental points have significant scattering at high temperature due to instabilities and contact phenomena. The results will be discussed in Section 4.3.

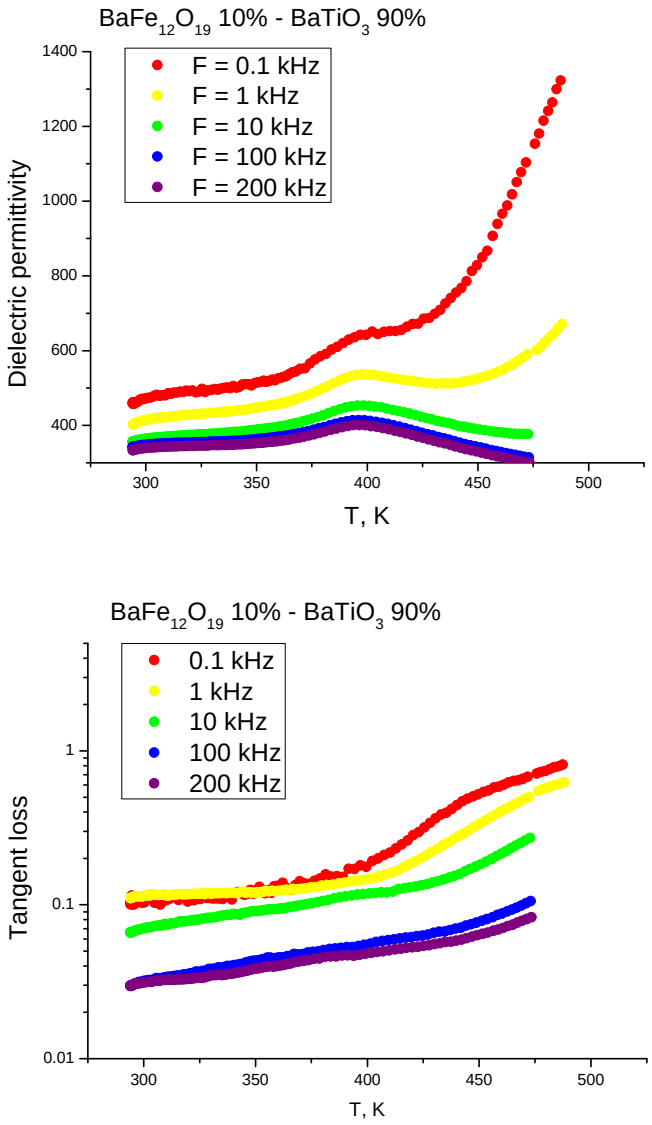

Fig 22. *Temperature dependence of dielectric permittivity and dissipation factor for $BaFe_{12}O_{19}$ 10% - $BaTiO_3$ 90%*

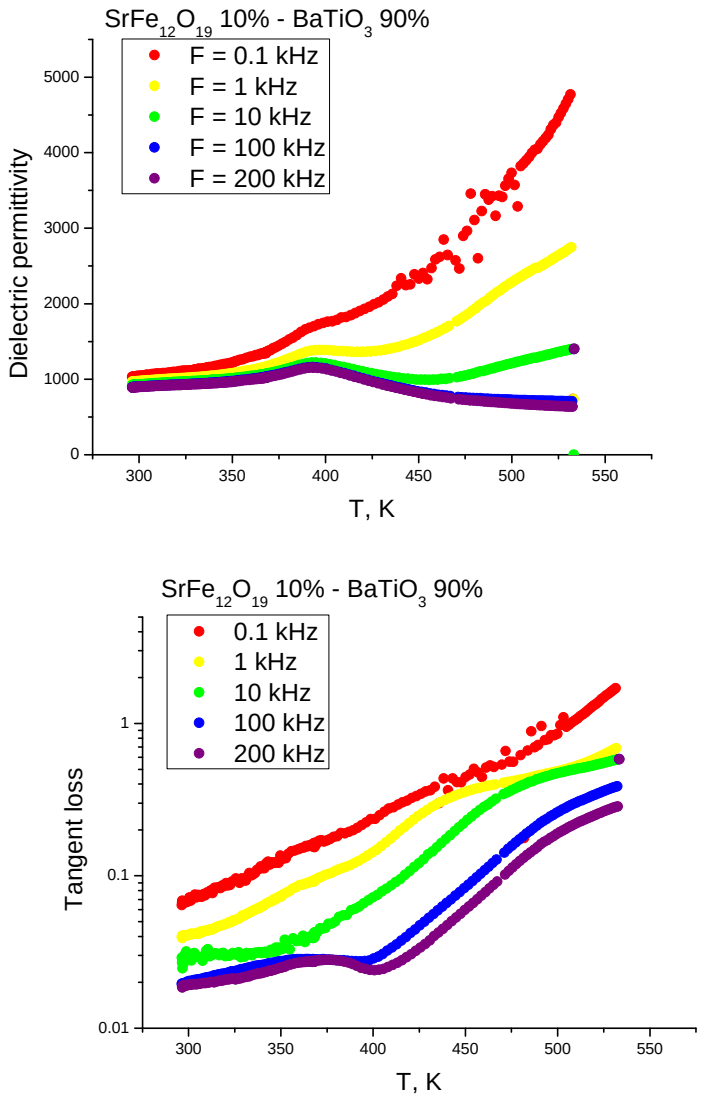

Fig 23. *Temperature dependence of dielectric permittivity and dissipation factor for $SrFe_{12}O_{19}$ 10% - $BaTiO_3$ 90%*

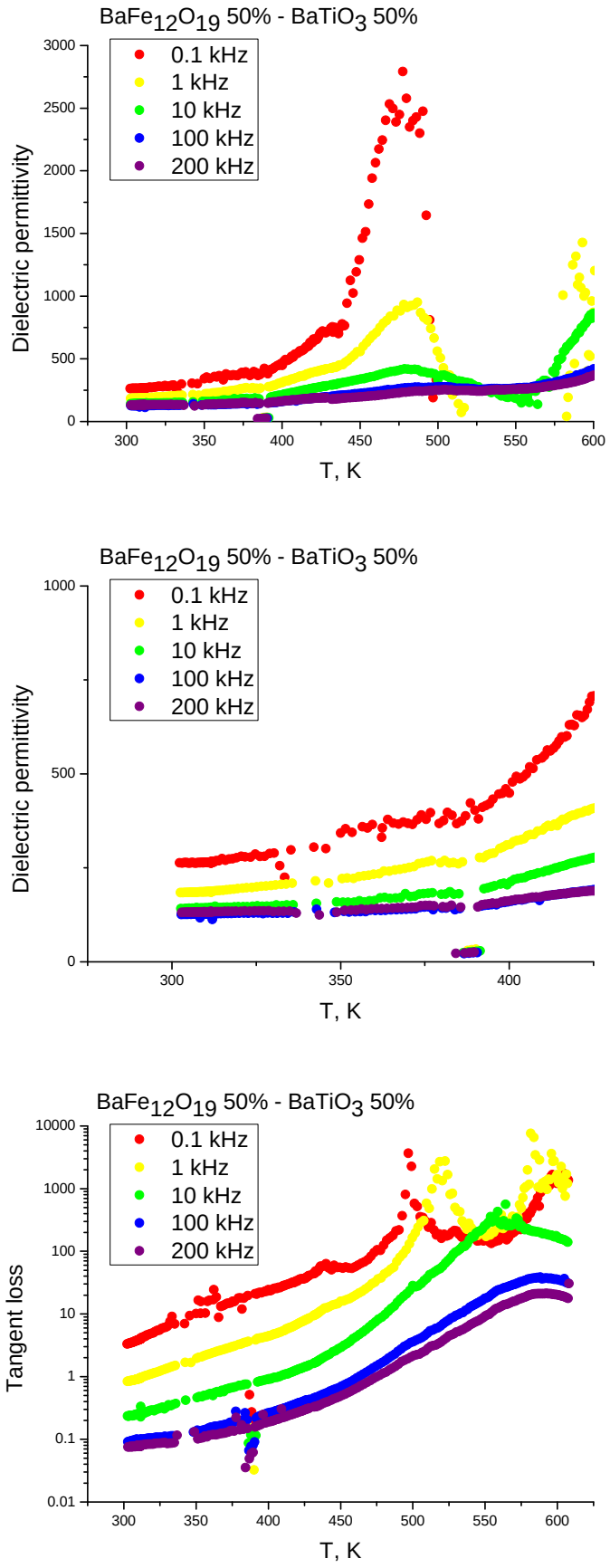

Fig 24. *Temperature dependence of dielectric permittivity and dissipation factor for $BaFe_{12}O_{19}$ 50% - $BaTiO_3$ 50%*

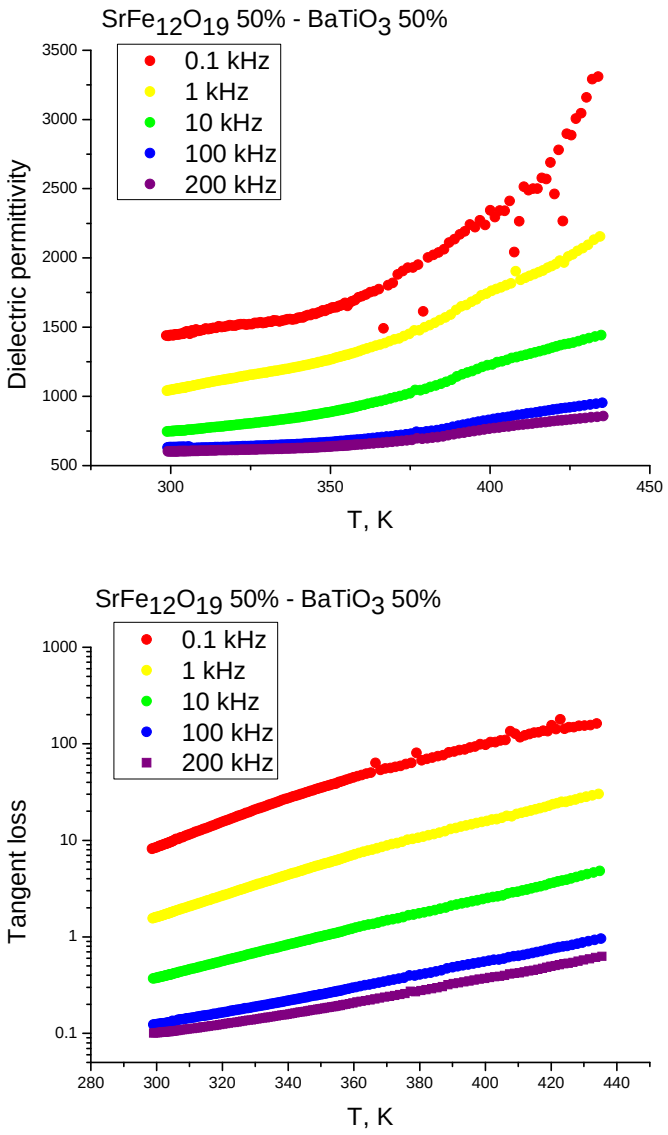

Fig 25. *Temperature dependence of dielectric permittivity and dissipation factor for $SrFe_{12}O_{19}$ 50% - $BaTiO_3$ 50%*

3.2.3. Magnetic measurements

Bulk magnetic properties of the samples were analyzed by means of vibrating-sample magnetometer (VSM).

A vibrating sample magnetometer (VSM) operates on Faraday's law of induction which states that an electromotive force (e.m.f.) will be generated in a coil when there is a change in flux linking the coil. For a coil with *n* turns we may write[48]:

$$E = -n\frac{d\Phi}{dt} \tag{7}$$

where *E* is an electromotive force, $d\Phi/dt$ – rate of change of the magnetic flux.

Considering that the magnetic flux $d\Phi$ through a surface element *dA* is defines as $d\Phi = BdA$, where *B* is the magnetic flux density, Eq. (7) can be presented as:

$$E = -na\frac{dB}{dt} \tag{8}$$

where *a* is cross-section area of the coil.

If the coil is positioned in a constant magnetic field, one has

$$B = \mu_0 H \tag{9}$$

where *H* is magnetic field strength.

When we bring a sample having a magnetization *M* into the coil, we have

$$B = \mu_0 (H + M) \tag{10}$$

The corresponding flux change is

$$\Delta B = \mu_0 M \tag{11}$$

Combining Eqs. (8) and (11) leads to

$$Edt = -na\mu_0 M \tag{12}$$

This means that the output signal of the coil is proportional to the magnetization *M* but independent of the magnetic field in which the value of *M* is to be determined.

In VSM, the sample is subjected to a sinusoidal motion (frequency ν) and the corresponding voltage is induced in a suitably located stationary pickup coils. The electrical output signal of these latter coils has the same frequency ν. Its intensity is proportional to the magnetic moment of the sample, the vibration amplitude, and the frequency ν. A simplified schematic representation of the VSM is given in Fig. 26. The sample to be measured is centered in the region between the poles of the laboratory magnet, able to generate the measuring field H_0. A thin vertical sample rod connects the sample holder with a transducer assembly located above the magnet. The transducer converts a sinusoidal ac drive signal, provided by an

oscillator/amplifier circuit, into a sinusoidal vertical vibration of the sample rod. The sample is thus subjected to a sinusoidal motion in the uniform magnetic field H_0.

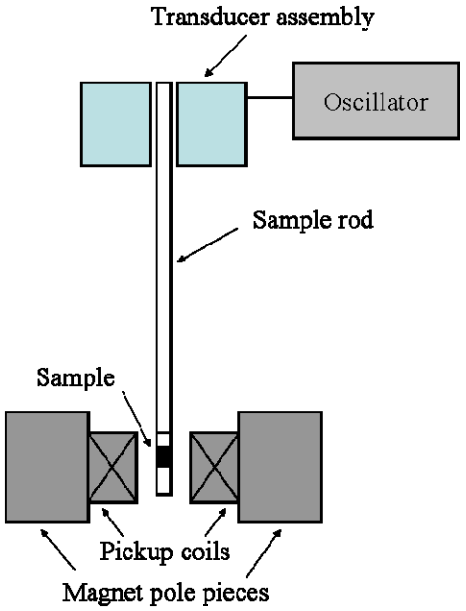

Fig 26. *Schematic representation of a VSM*

The temperature dependence of magnetization was acquired in Cryogen free VSM (Cryogenic™) having the following technical characteristics:

- Sample vibration frequency: 1 to 100 Hz
- Sensitivity: up to 10^{-6} emu with a suitable averaging time
- Temperature range: 1.6 K to 325 K
- Magnetic field: up to 18 T

The system is operated by means of LabView software.

The image of the system and its detailed structure is given in Fig. 27:

The magnetic hysteresis loop acquisition was performed at room temperature in Oxford Instruments VSM equipped with the furnace. The system had following technical characteristics:

- Sample vibration frequency: 40 Hz
- Sample vibration amplitude 1.5 mm
- Sensitivity: up to 10 emu/V
- Temperature range: from room temperature to 1000 K
- Magnetic field: up to 1 T

(a) (b)

Fig 27. *Cryogenic™ VSM equipment (a) outward view, (b) structure (Source www.cryogenic.co.uk)*

The following magnetic measurements were performed: 1) temperature dependence of magnetization M(T) at constant magnetic field for the 50% - 50% compositions in the temperature range 50 – 300K. 2) magnetic hysteresis loop acquisition M(B) at room temperature. The results are presented in Figs. 28 - 33

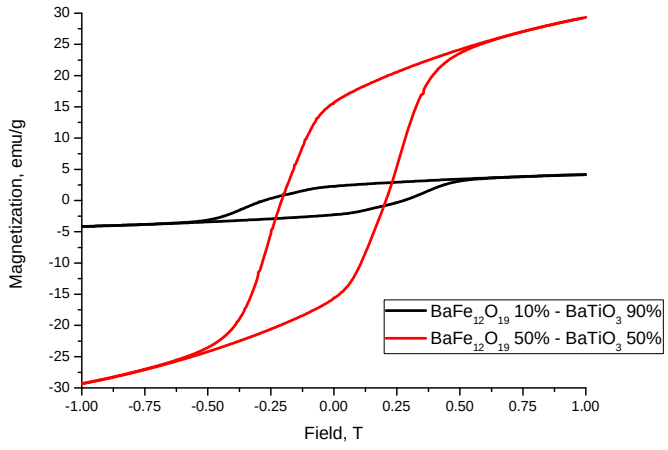

Fig 28. *Magnetization hysteresis of $BaFe_{12}O_{19}$ - $BaTiO_3$.*

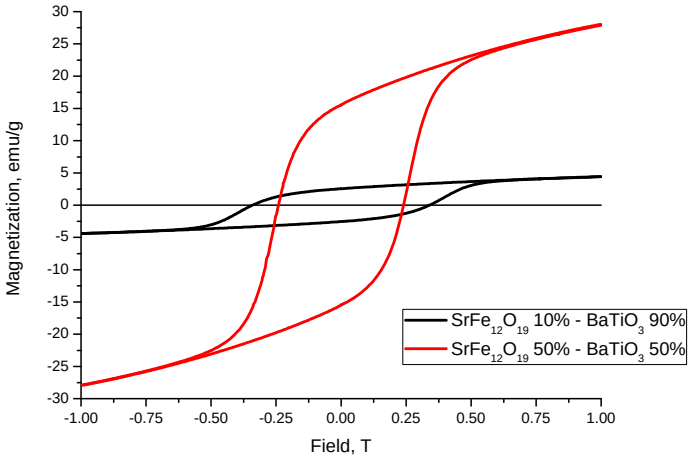

Fig 29. *Magnetization hysteresis of $SrFe_{12}O_{19}$ - $BaTiO_3$*

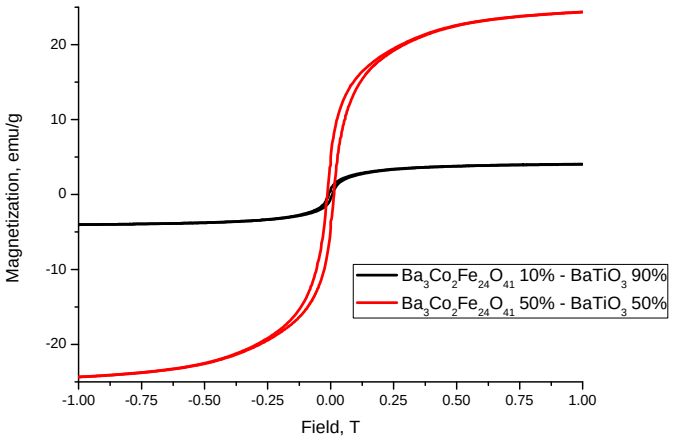

Fig 30. *Magnetization hysteresis of $Ba_3Co_2Fe_{24}O_{41}$ - $BaTiO_3$*

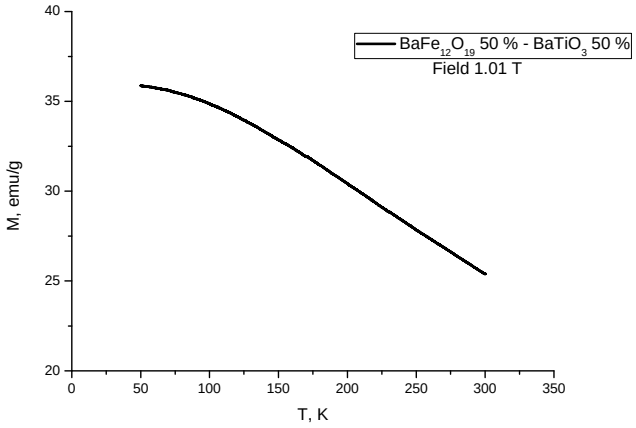

Fig 31. *Temperature dependence of $BaFe_{12}O_{19}$ 50% - $BaTiO_3$ 50% at magnetic field 1 T*

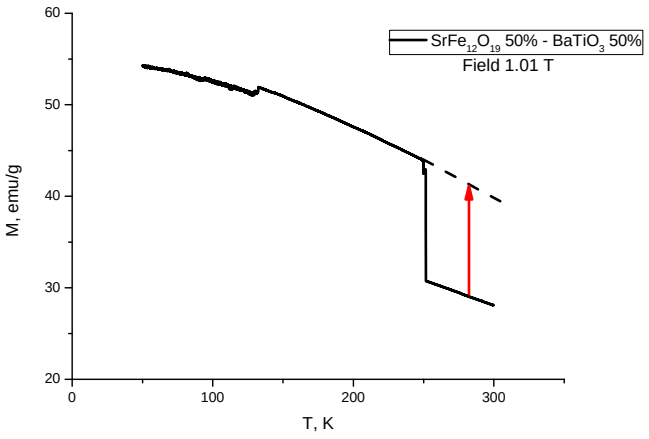

Fig 32. *Temperature dependence of $SrFe_{12}O_{19}$ 50% - $BaTiO_3$ 50% at magnetic field 1 T (dashed line- corrected)*

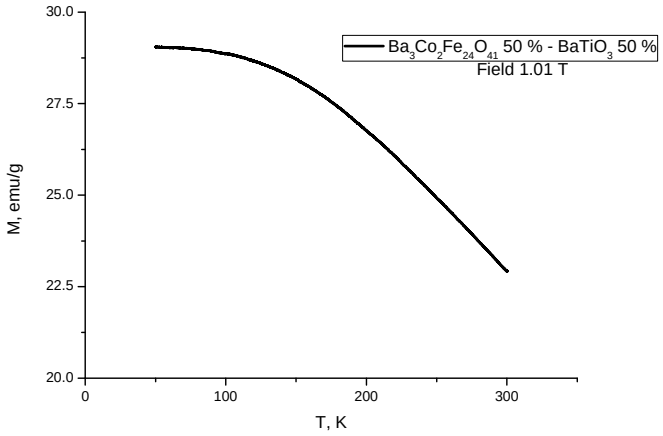

Fig 33. *Temperature dependence of $Ba_3Co_2Fe_{24}O_{41}$ 50% - $BaTiO_3$ 50% at magnetic field 1 T*

3.2.4. Analysis of nanoscale properties

Local piezoelectric and magnetic properties were studied by means of commercial atomic force microscope (Multimode, Nanoscope IIIA, Veeco™) (Fig 34).

Fig 34. *Atomic force microscope Nanoscope IIIA, Veeco™*

The principle of atomic force microscopy is simple: a tip of nanometer scale sharpness is mechanically contacted with the surface to probe the morphology. High instrument resolution is obtained using a very sharp silicon nitride probe. The sample is mounted under the probe and it is moved in X, Y and Z directions by a ceramic piezo-scanner. The tip is mounted on the edge of an elastic cantilever (100-200 μm) of low spring constant to keep the probe in contact with surface. Deflection of the tip along Z axis, due to different height on the surface of the sample, is monitored by an optical laser. With all this information it is possible to obtain a 3D scan of the surface.

For the piezoelectric measurements the microscope was equipped with an external lock-in amplifier (SR-830, Stanford Research) and a function generator (FG120, Yokogawa), which were used to apply the ac and dc voltages to the sample surface for poling, imaging, and local piezoelectric hysteresis loop acquisition[49]. The amplitude and frequency of the ac voltage were 1–2 V and 50 kHz, respectively. The dc voltage varied from zero to ± 30 V and was applied to the tip kept at a fixed position. Stiff conducting Si cantilevers (42 Nm^{-1}, PPP-NCHR, Nanosensors) were used for the measurements performed in ambient environment. The tip-cantilever system is made of n^+ – silicon with resistivity 0.01 – 002 Ωcm and has aluminium coating on reflecting side. The tip has the shape of a polygon-based pyramid with the height of 10-15 μm and the radius $r_{tip} \approx 10$ nm at the apex.

For the magnetic measurements the microscope was equipped with hard magnetic cantilevers (2.8 Nm^{-1}, PPP MFMR, Nanosensors). The tip-cantilever system is made of n^+ –

silicon with resistivity 0.01 – 0.02 Ωcm. It has a hard magnetic coating (coercivity of app. 300 Oe and remanent magnetization of app. 300 emu/cm^3) on the tip side and aluminium coating on detector side. The tip has the shape of a polygon-based pyramid with the height of 10-15 μm and the radius r_{tip} ≈10 nm at the apex.

3.2.4.1. Piezoresponse force microscopy (PFM)

The PFM method is based on monitoring piezoelectric surface displacements induced by the electrically biased probing tip[50]. This method was introduced in 1992 by Guethner and Dransfeld to detect polarized regions in ferroelectric copolymer film and, soon after that, proved to be the most effective approach for the nanoscale study and control of ferroelectric domains in bulk crystals and thin films.

The experimental setup is presented in Fig. 35:

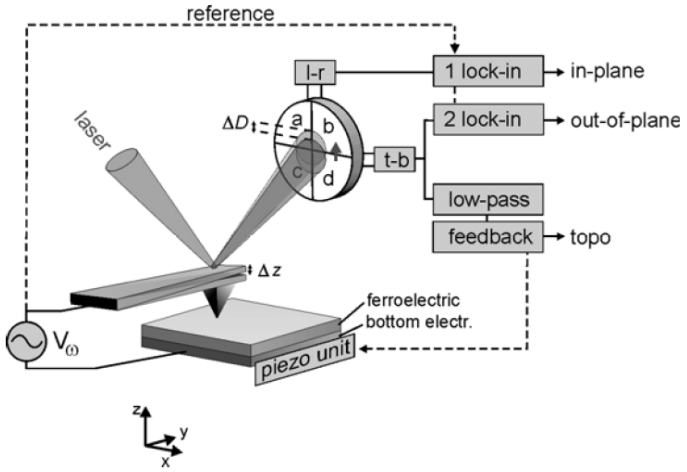

Fig 35. *PFM experimental setup for simultaneous acquisition of topography and vertical and lateral polarization components*

A ferroelectric sample under investigation is placed between the bottom electrode and the conductive PFM tip, serving as a movable top electrode. An ac voltage V_ω is applied between electrode and tip. This results in sample surface oscillations due to the converse piezoelectric effect.

The microscope is operated in a contact mode. Thus, the normal deflection of the cantilever is kept constant by the feedback while scanning. The feedback loop is adjusted to be slow enough to follow the oscillations caused by the electromechanical deformation at the frequency of the ac voltage. It will follow any topographical features, however. The actual

position of the cantilever represents the topography and is acquired by the control electronics. The first harmonic of the cantilever oscillations results from the piezoelectric response.

If the spontaneous polarization is normal to the surface, the sample is periodically contracted and expanded through the inverse piezoelectric effect. This results in a vertical movement of the laser spot in photo detector (Fig 36a). The magnitude A and phase φ of the cantilever oscillation is measured by a lock-in amplifier. The magnitude A is proportional to the absolute value of the effective piezoelectric coefficient d_{eff}. The term "effective" means, that the response will be clamped by the surrounding not exposed to the same electric field. The surface oscillation is nearly in phase ($\varphi \approx 0$) with the ac voltage for positive d_{eff} and in counter phase ($\varphi \approx 180°$) for negative d_{eff}. The deviation comes from the phase shifts due to mechanical delays caused by the inertia of the cantilever and from the electronics. It is compensated by adjusting the reference phase of the lock-in amplifier. From the measured sign of the piezoelectric coefficient in the laboratory system and the known sign of the crystal coordinate system the direction of the spontaneous polarization can be deducted.

Topographical features result in normal deflections of the cantilever and a vertical movement of the laser spot too. With the feedback adjusted so as not to follow any movements at frequency ω or above, a pure topography signal is obtained easily.

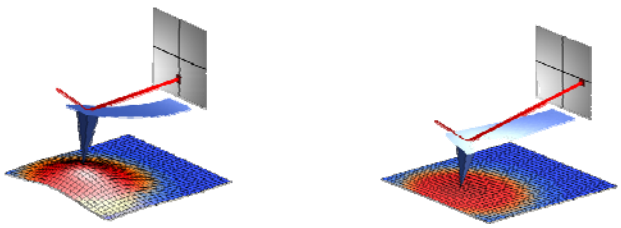

(a) (b)

Fig 36. *Schematic representation of vertical and lateral PFM (source: S. Kalinin "Piezoresponse force microscopy: Instrumentation, Theory and Applications", Oak Ridge National Laboratory)*

In the case when the spontaneous polarization is aligned in the plane of the sample, there will be no oscillations normal to the surface, since the corresponding coefficient vanishes. However, the crystal will shear locally resulting in a lateral oscillation of the tip. Again the direction of the shear depends on the direction of the spontaneous polarization. The movement of the crystal is transferred to the tip by friction. This results in a horizontal movement of the laser spot in photo detector (Fig 36b). The signal is then analyzed with lock-in amplifier with proper phase settings to extract the oscillation amplitude. From the phase of the lateral oscillation and

the known sign of the piezoelectric coefficient in the crystalline coordinate system the direction of the spontaneous polarization parallel to the sample surface can be deduced[51].

3.2.4.2. Local piezoelectric hysteresis loop acquisition

Along with the ferroelectric domain imaging PFM can be used in a spectroscopy mode when the measurements are done on a fixed tip position. This allows measurement of the piezoelectric coefficient as a function of the dc field (local d_{33} acquisition). The dependence of the local piezoelectric vibration on applied bias is referred to as a piezoelectric hysteresis loop. In addition to the conventional PFM configuration (Fig. 35), a dc bias is applied to the sample.

There exist two fundamentally different ways to apply the poling field. In the first one the field is applied all the time and its strength is slowly cycled. Positive voltages on the electrode will tend to switch the polarization upwards and negative downwards. The piezoelectric response is probed continuously with the poling field switched on, resulting in a continuous curve (Fig. 37a). Such loops are called in-field loops.

As an alternative, a sequence of voltage pulses of a certain duration τ but increasing/decreasing voltage U_0 are applied. After each pulse the system is given several seconds to stabilize (time constants of lock-in amplifier below 100 ms). Then the piezoresponse is measured. The measured signal is plotted as a function of the voltage of the last applied pulse (Fig. 37b). This results in curves showing the remanent converse piezoelectric response of the sample after poling. Consequently, these loops are called remanent hysteresis loops.

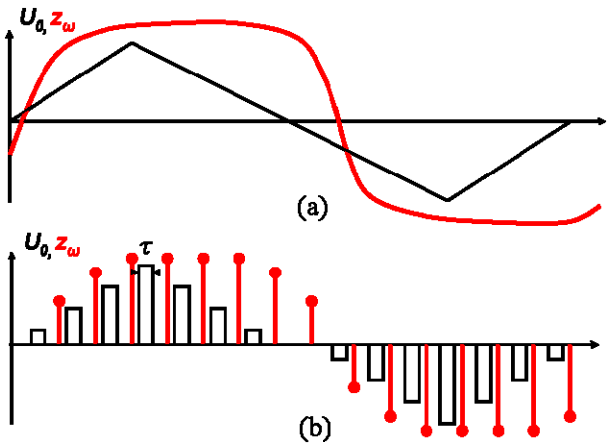

Fig 37. *Functions of the dc voltage applied during the local piezoelectric hysteresis measurements (a) cycled, (b) pulsed*

3.2.4.3. Magnetic force microscopy (MFM)

The MFM method is based on the detection of cantilever deflection and/or a change in its resonance frequency and phase, which results from the interaction between the tip and the fringe field above the sample[52] as shown in Fig. 38.. This method was first proposed by Y. Martin and H.K. Wickramasinghe in 1987[53] as one of the applications of the atomic force microscope (AFM) invented one year earlier.

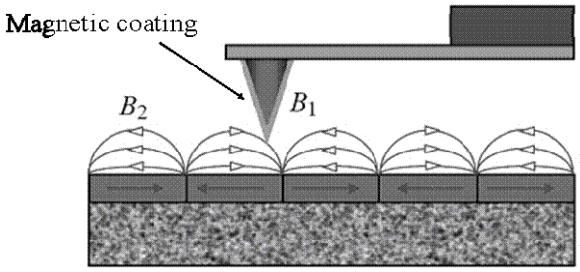

Fig 38. *Principle of the magnetic domains imaging*

Today, there are two modes of the MFM operation: static MFM and dynamic MFM. In the static MFM mode (dc), the interaction force F is measured through the detection of the cantilever deflection Δz from the equilibrium position which is given by

$$\Delta z \approx \frac{F}{k} \tag{13}$$

where k – cantilever spring constant.

In the dynamic MFM mode (ac), the change in resonant properties of the vibrating system cantilever-sample is registered. In this case the amplitude A, phase φ and resonant frequency ω_0 of the cantilever oscillation must be detected. If the force with the gradient $\partial F/\partial z$ acts on the cantilever in the vibration direction z, the above mentioned parameters variation can be expressed as

$$\Delta\phi \approx \frac{Q}{k}\frac{\partial F}{\partial z} \tag{14}$$

$$\Delta A \approx \left(\frac{2A_0 Q}{3\sqrt{3k}}\right)\frac{\partial F}{\partial z} \tag{15}$$

$$\Delta\omega_0 \approx -\frac{1}{2k}\frac{\partial F}{\partial z}\omega_0 \tag{16}$$

where k – cantilever spring constant, Q – vibrating system quality factor, A_0 – amplitude of cantilever oscillation at resonant frequency ω_0 in the absence of external force gradient. As can be seen from (14) – (16), all three experimentally determined parameters are linear functions of the force derivative. In practice, however, $\partial F/\partial z$ is mainly determined by measuring the cantilever phase variation.

In magnetic investigations on submicron scale first of all one must separate the magnetic image from the topography. To solve this problem the magnetic measurements are executed by means of two-pass method. In the first pass the topography is determined in contact or semicontact mode. In the second pass the cantilever is lifted to a selected height for each scan line (or after topography measurement), and scanned using the stored topography (without the feedback). As a result the tip-sample separation during second pass is kept constant. This tip-sample separation must be large enough to eliminate the Van der Waals' force. During second pass the short-range Van der Waals' force vanishes and the cantilever is affected by long-range magnetic force. Both the height-image and the magnetic image are obtained simultaneously with this method[54].

Piezoresponse and magnetic force microscopies were performed for all the compositions. The aim was to take the PFM and MFM images at the same place. In such a case not only the general information about the ferroelectric and magnetic domain structure can be obtained, but also we are able to distinguish between ferroelectric and magnetic grains: the former were not supposed to be detected by MFM, while the latter should not produce any piezoresponse.

Figs. 39, 41, and 43 represent PFM and MFM images taken at the same place together with the topography for the following composites: $SrFe_{12}O_{19}$ 10% - $BaTiO_3$ 90%, $Ba_3Co_2Fe_{24}O_{41}$ 10% – $BaTiO_3$ 90%, and $Ba_3Co_2Fe_{24}O_{41}$ 50% – $BaTiO_3$ 50%. Figs. 40, 42, and 44 presenting the superposition of the PFM and MFM images in Figs. 39, 41, and 43 respectively, are given in order to show the correlation and magnetoelectric coupling between the two phases. The PFM images scale is given in volts, however, these units should be considered as arbitrary (but proportional to the effective piezoelectric coefficient and thus to polarization). Such representation is connected to the fact that the piezoresponse is acquired by means of external lock-in amplifier. The effective signal coming from the lock-in output in volts was then transferred to the image through the microscope control box input. In fact, the signal connected to the topography is also detected in volts. However, it is further converted into real displacements by the calibration files in the computer. The calibration of the PFM was not performed in the current work.

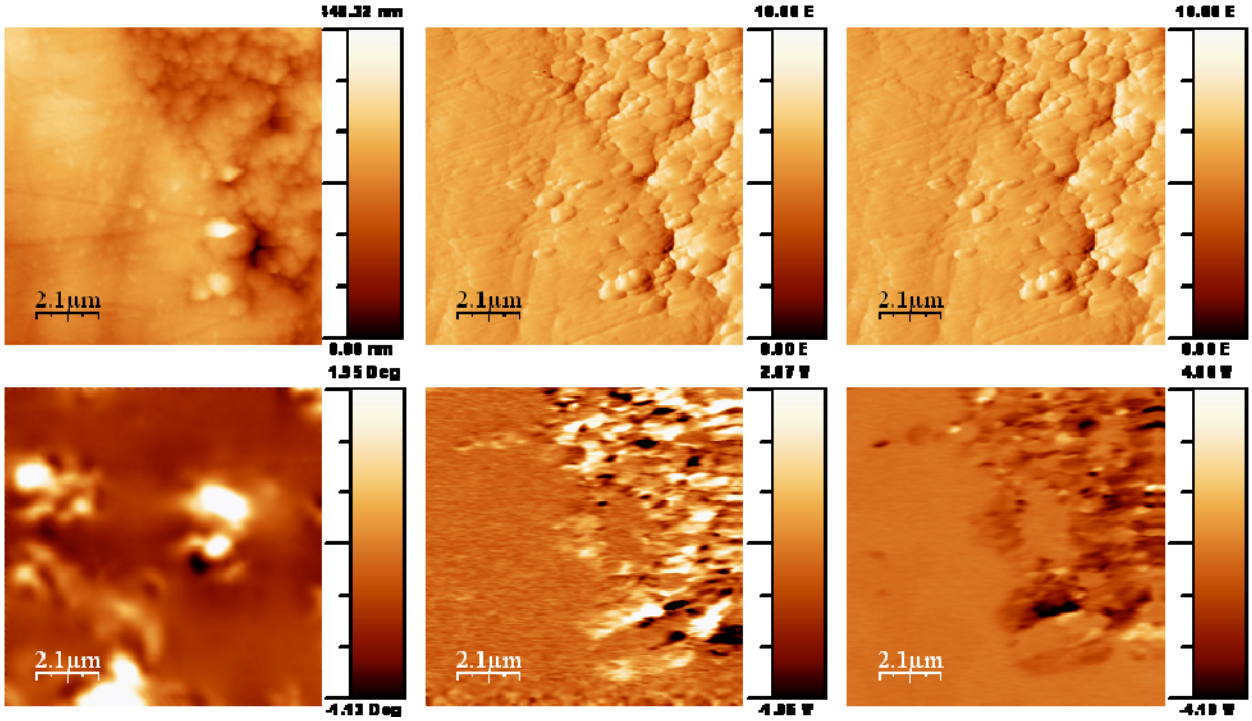

(a) (b) (c)

Fig 39. *MFM (a), vertical (b) and lateral (c) PFM images with corresponding topographies for $SrFe_{12}O_{24}$ 10% – $BaTiO_3$ 90%.*

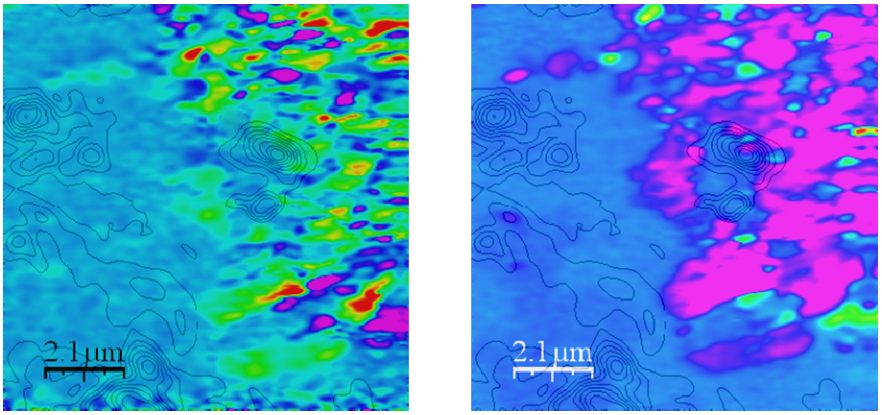

(a) (b)

Fig 40. *Superposition of (a) MFM and lateral PFM (b) MFM and vertical PFM for $SrFe_{12}O_{19}$ 10% – $BaTiO_3$ 90%*

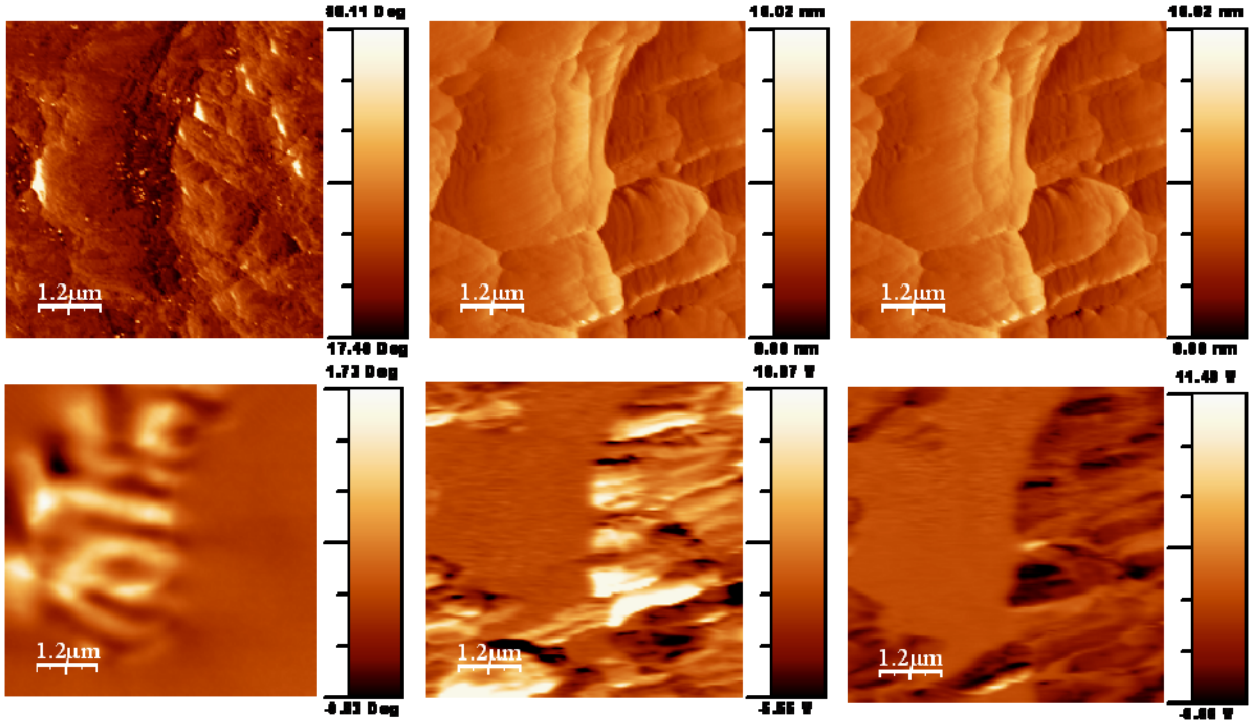

(a) (b) (c)

Fig 41. *MFM (a), vertical (b) and lateral (c) PFM images with corresponding topographies for $Ba_3Co_2Fe_{24}O_{41}$ 10% – $BaTiO_3$ 90%.*

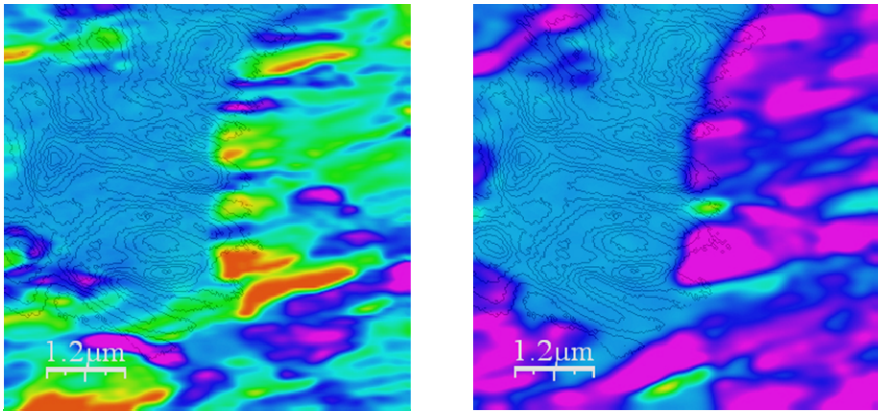

(a) (b)

Fig 42. *Superposition of (a) MFM and lateral PFM (b) MFM and vertical PFM for $Ba_3Co_2Fe_{24}O_{41}$ 10% – $BaTiO_3$ 90%*

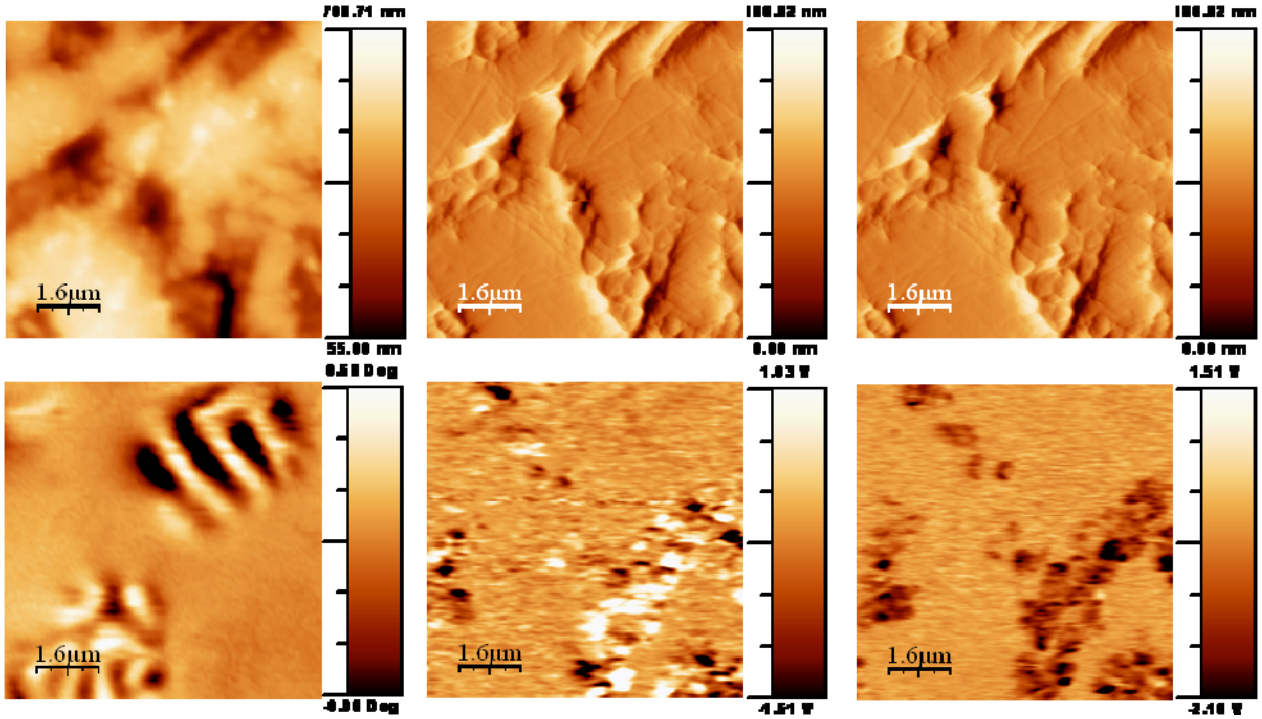

(a) (b) (c)

Fig 43. *MFM (a), vertical (b) and lateral (c) PFM images with corresponding topographies for* $Ba_3Co_2Fe_{24}O_{41}$ *50% –* $BaTiO_3$ *50%.*

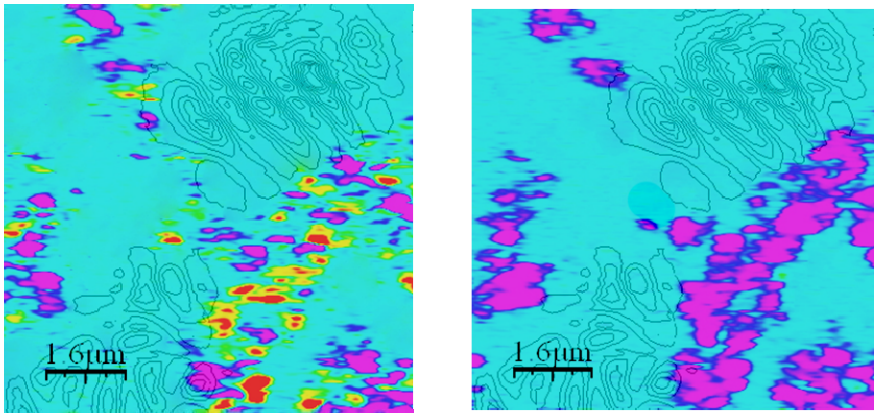

(a) (b)

Fig 44. *Superposition of (a) MFM and lateral PFM (b) MFM and vertical PFM for* $Ba_3Co_2Fe_{24}O_{41}$ *50% –* $BaTiO_3$ *50%*

The local hysteresis loop acquisition was performed for $SrFe_{12}O_{19}$ – $BaTiO_3$ composition in continuous dc mode. The data together with the reference curve (pure $BaTiO_3$) is presented in Fig. 45

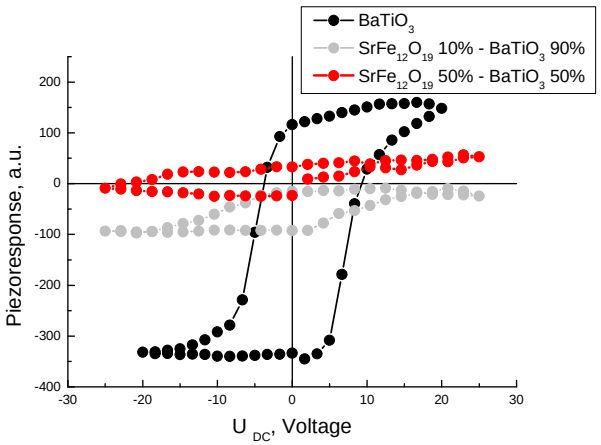

Fig 45. *Local ferroelectric hysteresis loops in $SrFe_{12}O_{19}$ – $BaTiO_3$ composites*

As we could see, the ferroelectric hysteresis loops are shifted along y-axis for both pure barium titanate, and the 10%-90% composition. The nature of the shift along y-axis was clarified by S. Hong *et al.*[55]. According to their model, the collected PFM signal is determined by both, the piezoelectric vibration of the surface and by the electrostatic (Maxwell) force between the cantilever and the sample and can be described by the following equation:

$$A\cos\phi = -\frac{2K\Gamma_{lever}}{k_{lever}}(V_{dc}+V_c)V_{ac} \pm d_{33}V_{ac} \qquad (11)$$

where $\Gamma = \frac{1}{2}\frac{\partial C}{\partial z}$, C is the electric capacitance between the tip-cantilever system and the piezoelectric surface, k_{lever} – spring constant of the cantilever, and K – positive calibration constant smaller than unity. The first term in the right side of Eq. (11) is the capacitive contribution of the cantilever, whereas the second term is the piezoelectric contribution.

Neglecting the electrostatic interaction between the cantilever and the sample, the curves were replotted symmetrically as shown on Fig. 46:

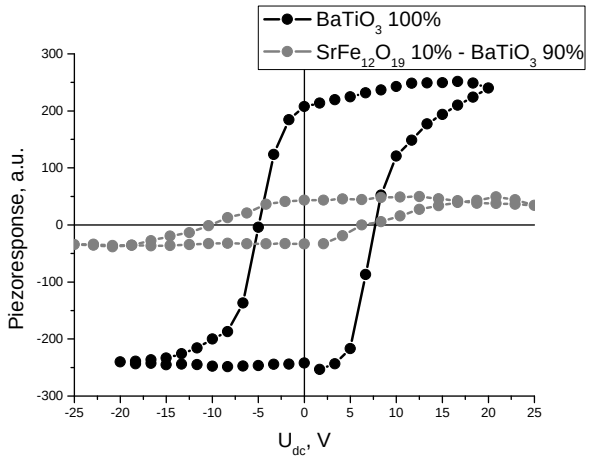

Fig 46. *Local ferroelectric hysteresis loops in $SrFe_{12}O_{19}$ – $BaTiO_3$ composites neglecting electrostatic interactions and shifts along vertical axis*

Weak hysteresis for 50%-50% composition is not shown because the response was not stable and differed from point to point.

3.2.4.4. Local electromagnetic coupling

The experiment was aimed to detect locally the coupling between polarization and magnetic switching in the adjacent grains. The idea was to observe a change (if any) in the magnetic domain configuration after the full switching of the ferroelectric grain next to it and thus prove that the mechanical stress exerted via grain boundary is responsible for the magnetoelectric effect typically observed in particulate composites. The investigated sample was $BaFe_{12}O_{19}$ 50 % – $BaTiO_3$ 50 % with well defined domains. The poling voltage of +90V was applied for 15 min to the point located at about 0.7 μm from the grain boundary with magnetic grain. The conductive tip was biased and scanned over a 0 x 0 μm^2 area in the contact mode. After the poling the piezoelectric grain was supposed to be expand/contract due to electrostriction $\Delta l = Q_{12}(P_r^2 - P_i^2)$ where P_r is the remanent polarization, P_i – initial (close to zero) polarization and Q_{12} – transverse electrostriction coefficient. Transverse electrostriction coefficient should be used instead of piezoelectric one. In case of a fully compliant grain it would lead to the strain of the order of 10^{-3} and deformation of 2-5 nm. This would cause appreciable changes of the magnetic domains and relevant total magnetic moment.

The PFM and MFM images of the same area were taken both before and after the poling. The results are presented in Figs. 47– 49

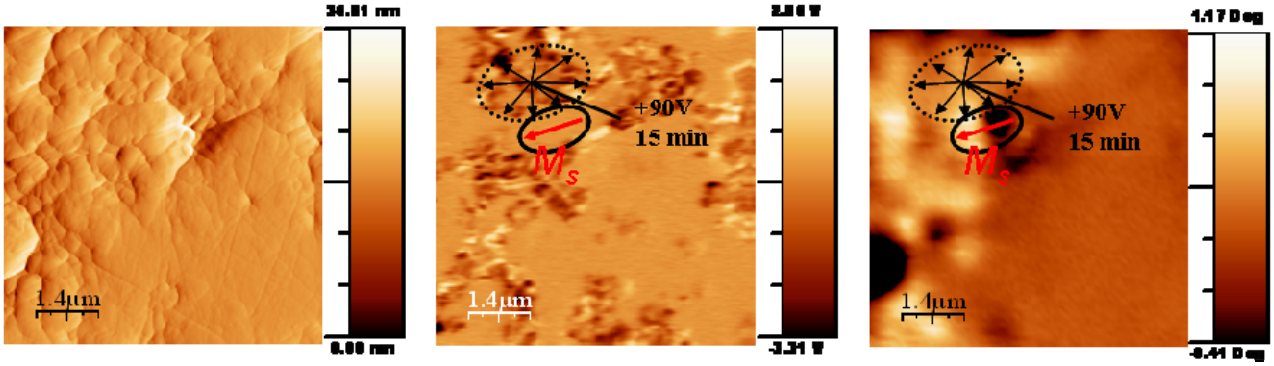

(a) (b) (c)

Fig 47. *Topography (a), vertical PFM (b) and MFM (c) images of $BaFe_{12}O_{19}$ 50 % – BaTiO3 50 % before poling. The arrow marks the point at which the voltage was applied.*

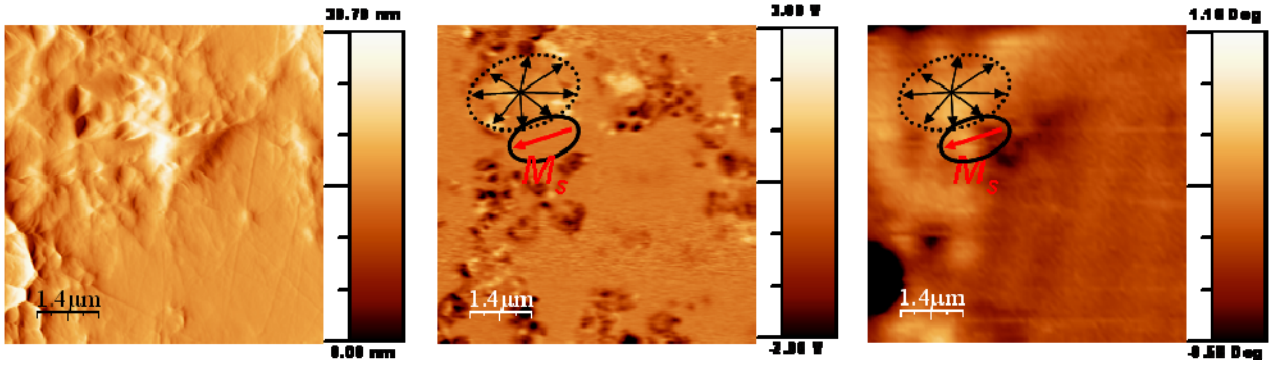

Fig 48. *Topography (a), vertical PFM (b) and MFM (c) images of $BaFe_{12}O_{19}$ 50 % – $BaTiO_3$ 50 % after poling. The arrow marks the point at which the voltage was applied.*

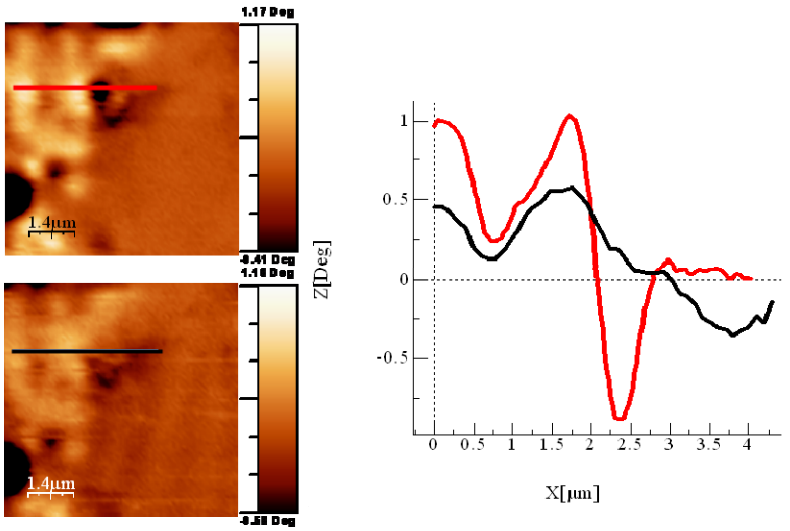

Fig 49. *Changes in the magnetic properties: red curve – cross-section of the region before the poling, black curve – cross-section of the region after the poling*

It can be noted that the topography did not significantly change but the ferroelectric grain acquired bright contrast, i.e. became fully polarized. The small changes of the grain boundary position could not be detected due to low resolution. It is well seen that the positions of the minimum and maximum contrast (corresponding to the domain wall and centre of magnetic domain) do not shift in the left part of image. However, significant changes are observed in the right part where the shift of the domain reached about 1.4 μm. Such a big shift is supposed to lead to a high local magnetoelectric effect of the order of $\Delta M/E_c$ where ΔM is the variation of the magnetic moment (close to remanent magnetization M_r and E_c is the coercive field).

4. RESULTS AND DISCUSSIONS

4.1. Phase distribution

Both SEM and AFM showed a good distribution of the parent phases in the samples with 50% - 50% compositions and agglomeration of the magnetic phase in the samples with 10% fraction of the ferrites.

In the AFM the phases could be distinguished due to the different contrast in PFM and MFM, as it was described in the experimental part. In SEM, owing to sufficient grain size of the components, the different phases could be distinguished simply by their shape. The magnetic phase, having a hexagonal unit cell symmetry, formed corresponding grains with hexagon edges, while ferroelectric phase, $BaTiO_3$, with the tetragonal, practically cubic symmetry (if we consider lattice parameters: 3.9945 Å for *a* and 4.01335 Å for *c*) formed grains with quite uniform shape. EDS analysis performed in the characteristic points confirmed this assumption. The ferroelectric phase had predominance of barium and titanium, while magnetic phases, all having high content of iron predominance over barium and titanium. However, some signal from the opposite phase (e.g. slight Fe peaks in the ferroelectric phase) could be also detected. This could be connected, first, to the lack of resolution of the EDS analysis, and, second, to the signal coming from the grains located under the under the measured one.

One may think that the topography image in the AFM could also give the information about the grain shape. However, in our case this does not work. Due to the micron dimensions of the tip, the AFM can be performed only on the surfaces with the roughness not exceeding ≈1 μm. Measurements on the surfaces with the roughness higher than 1 μm will result in the damage of the cantilever, not to mention cross-talk between topography and measured property. If we take a look at the SEM images, it is clear that the smallest grains of the magnetic phase are over 1 μm. Therefore, polishing till the surface roughness less than 1 μm had to be done before performing AFM experiments. In this case though the surface was almost flat, the information about the grain configuration and location of grain boundaries is apparently lost.

Agglomeration of the magnetic phase in the compositions with 10% ferrite fraction could be connected to insufficient dispersion of the ferrite particles during mixing. Being very strong magnets (the samples were attracted by the external magnets) they could stick to each other and remain together even while sintering. During sintering they were likely to agglomerate forming very large magnetic grains. The “champion” among the three different compositions was composite with 10% of cobalt Z-ferrite. Some of the formed grains in longitude exceeded 50 μm.

The consequences of the magnetic phase agglomeration to magnetoelectric effect are rather negative. The larger is the grain, the lower will be its surface area comparing to the same amount of material with a smaller grain size. The total surface in its turn would determine the area where the two phases can connect to each other. Since the most common mechanism of magnetoelectric coupling is connected to piezoelectricity/magnetostriction, the connection between two phases becomes really essential. Without good phase connectivity, the expansion/contraction of one phase would affect much the geometry of the spurious phase. As the result, the magnetoelectric coupling will be weaker or even vanish at all.

4.2. Changes in the unit cell parameters

Changes in the unit cell parameters of the composite components have been already studied by several groups. Chang-Dae Oh *et al.*[56] working with the $BaTiO_3$ – $K_3Li_2Nb_5O_{30}$ composites reported large changes especially in the *c* parameter in the tungsten bronze structure accompanied by relatively slight changes in both unit cell parameters of the perovskite structure. A group of B. K. Chougule[57] studied $BaTiO_3$ – $Ni_{0.03}Co_{0.02}Mn_{0.05}Fe_2O_4$ composites observed unit cell changes in both phases appeared at certain threshold composition, namely at perovskite phase fraction of 55%, both lattices showing an increase in the *a* parameter. However, in the work of R. S. Devan *et al.*[58], who investigated $BaTiO_3$ – $Ni_{0.93}Co_{0.05}Fe_2O_4$ composites, lattice parameters of both phases remained practically unchanged in all of the compositions (15, 30, and 45% fraction of the ferrite phase)

In present work, since only one fraction (50% - 50%) could be studied, the comparison was made only for the pure materials.

In the case of composites consisting of barium and strontium ferrite, the unit cell of the magnetic phase expanded. This in its turn led to the contraction of the ferroelectric phase of the composites. In the case of cobalt Z-ferrite, the situation was opposite. The magnetic phase was contracted in the composite. At the same time the ferroelectric phase in this composite is expanded. Such a coordinated behavior, expansion of one phase with simultaneous contraction of another and vise versa, indicates a quite good connectivity between the two phases.

Considering the effect on ferroelectric properties of the composites, the observed trend leads to gradual loss of ferroelectricity. It is known that the origin of ferroelectricity is asymmetric distribution of ions in the unit cell structure, which leads to separation of positive and negative charges within the cell and dipole formation. In our case, as we can better see in Fig 50, the *a* parameter of the ferroelectric phase is increased while *c* parameter is decreased

compared to the pure barium titanate phase. This means that the structure is verging towards cubic state and ferroelectricity is suppressed.

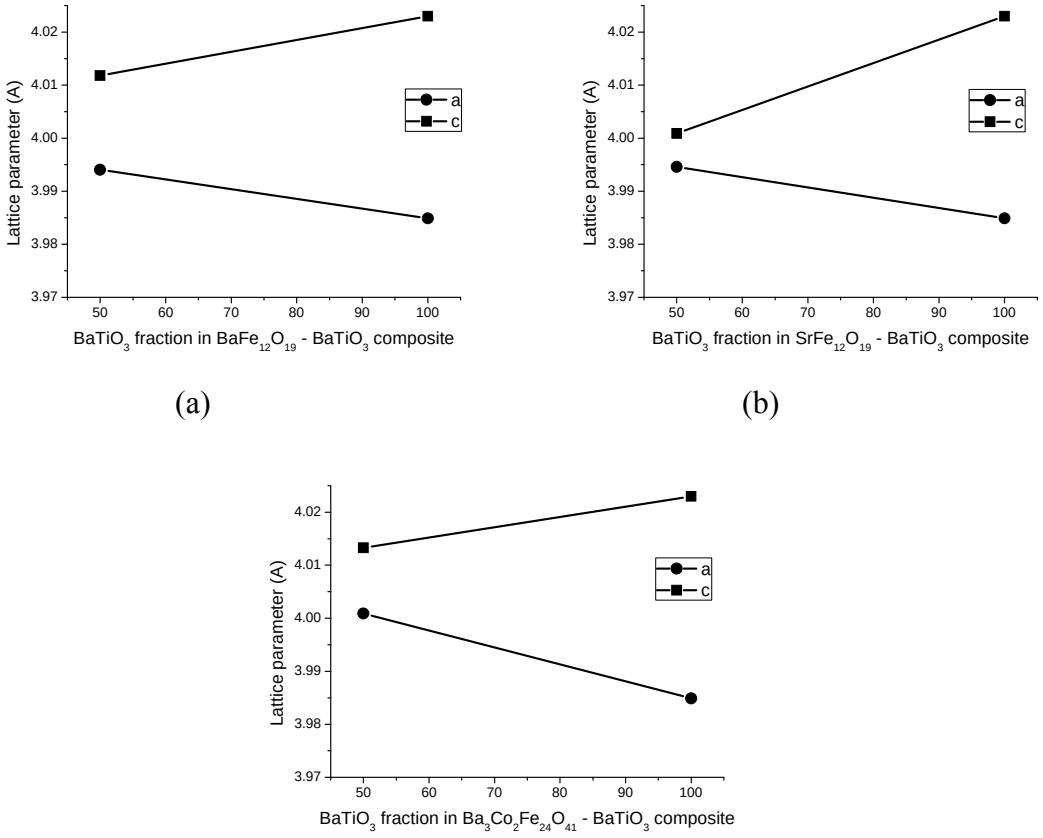

Fig 50. *Lattice constants of the perovskite phase in the composites (a) $BaFe_{12}O_{19} – BaTiO_3$; (b) $SrFe_{12}O_{19} – BaTiO_3$;(c) $Ba_3Co_2Fe_{24}O_{41} – BaTiO_3$*

The effect of the modified structure on the magnetic properties is not that clear. Magnetism originates from the cooperative action of non-compensated spins on the upper electronic shell, which are considered as small magnetic dipoles. As in the case of ferroelectrics, the crystallographic structure of the compound plays a big role in determining of the spin direction. However, there are also such factors like spin-orbital interactions, spin-spin interaction, etc, which may affect the macroscopic moment. As a proof of this it is enough to consider the studied compounds. Both M- and Z-ferrites has hexagonal symmetry of the unit cell, but the direction of magnetization in M-ferrites is parallel to the *c*-axis, while in Z-ferrites at room temperature the magnetization vector lies in the basal plane. Therefore, it is hard to say whether the structural changes would be favorable for the magnetic properties of the composites. The detailed discussion of the magnetic properties will be given in Section 4.4.

4.3. Dielectric properties

The frequency dispersion of the dielectric permittivity of $BaFe_{12}O_{19}$10% – $BaTiO_3$ 90% was studied at room temperature (Fig 21). It represents a linear dependence in the semi-log scale and is typical for ferroelectrics with a broad distribution of the relaxation times.[59] The apparent decrease of the permittivity with frequency is actually a superposition of multiple Debye relaxations due to the presence of defects or domain wall motion. [55] The increase of loss tangent with decreasing frequency can be attested to the increase of dc conductivity σ due to σ/ω term in the imaginary part of the dielectric permittivity.[59] Low frequency permittivity value is comparable with that for pure $BaTiO_3$ sample where a similar weak relaxation is observed.

Figs. 22-25 compare temperature dependencies of the effective dielectric permittivity and loss tangent in $SrFe_{12}O_{19}$10% – $BaTiO_3$ 90% and $BaFe_{12}O_{19}$10% – $BaTiO_3$ 90% samples as a function of temperature. It is seen that the relatively weak dispersion at room temperature (in both samples) is dramatically increased with increasing temperature. It is also a result of enhanced *ac* conductivity at high temperature. Nevertheless, the maximum of the permittivity was observed at about 390 K (temperature of the cubic to tetragonal phase transition in $BaTiO_3$). It signifies that the ferroelectric property is retained in all samples with high volume fraction of the ferroelectric phase. This transition is sufficiently broad and its diffuse character may be a result of the broad distribution of the grain sizes and the composite effect of the magnetic phase on the effective dielectric properties. It is worth noting the existence of another maximum of loss tangent at higher temperatures. This can be related to the relaxation of space charges accumulating at the magnetic-ferroelectric interface (Maxwell-Wagner effect). This should have a pronounced effect on magnetoelectric coupling if it is related to the interface properties. $SrFe_{12}O_{19}$ 10% – $BaTiO_3$ 90% sample exhibit much higher low-frequency permittivity. This can be attributed to higher porosity in these samples. Figs. 24 and 25 represent the relaxational properties of both $SrFe_{12}O_{19}$50% – $BaTiO_3$50% and $BaFe_{12}O_{19}$50% – $BaTiO_3$50% materials. The increase of the volume fraction of $SrFe_{12}O_{19}$50% has led to drastic increase of the room temperature relaxation of the permittivity and loss tangent (by the order of magnitude). It means that the conductivity contribution is much higher in these samples. Ferroelectric phase transition is almost not seen and can be smeared out due to the stresses and apparent effect of the magnetic phase. Different behaviour is observed in $BaFe_{12}O_{19}$50% – $BaTiO_3$50% composition. It exhibits a peak in the permittivity at about 475 K that is too high to be associated with the ferroelectric phase transition temperature. It can be due to the Maxwell-Wagner relaxation in these samples. The maximum is shifted to higher temperatures with increasing frequency as normally observed

in composite magnetoelectric materials (see, e.g.,[60]). Low-frequency permittivity in these samples is strongly reduced in accordance with mixing rules and most composite models.

4.4. Magnetic properties

The analysis of magnetic hysteresis loops showed different values of both magnetization saturation value and the coercive field depending on the amount of the magnetic phase. The results are summarized in Table 4.

	Percentage of ferrite	M_S, *emu/g*	H_C, *mT*
$BaFe_{12}O_{19}$+$BaTiO_3$	100%[18]	58.4	503.9
	50%	29.2	207.0
	10%	4.16	276.7
$SrFe_{12}O_{19}$+$BaTiO_3$	100%[18]	65.0	552.9
	50%	28.0	241.1
	10%	4.42	342.3
$Ba_3Co_2Fe_{24}O_{41}$+$BaTiO_3$	100%[19]	48.6	6.72
	50%	24.3	13.7
	10%	4.05	7.80

Table 4. *Changes in the magnetization saturation and coercivities as a function of the ferrite fraction*

The variation of the magnetization saturation showed practically linear dependence on the amount of the magnetic phase (Fig. 51).

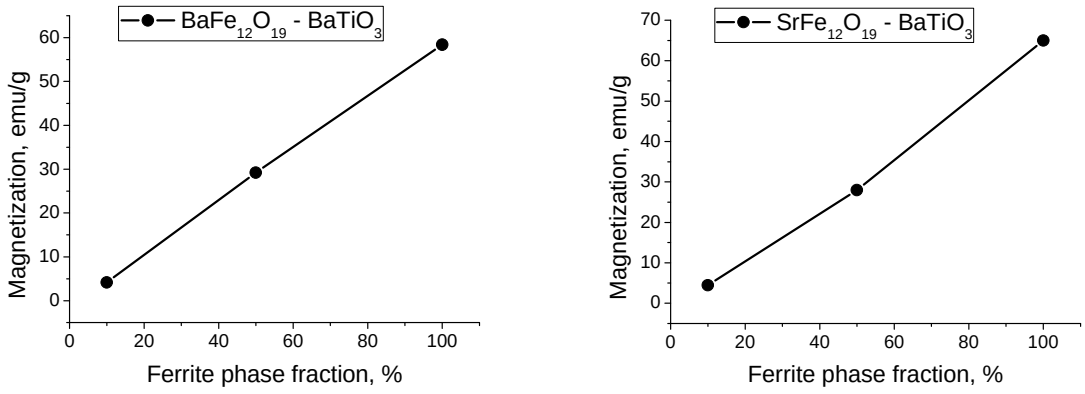

(a) (b)

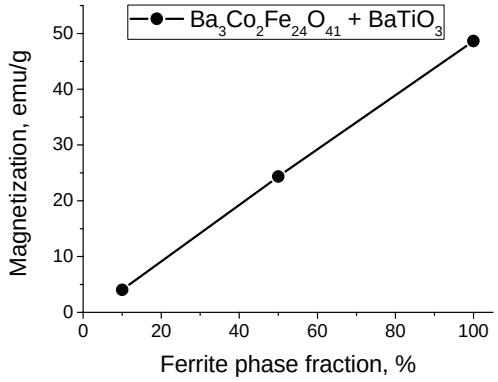

(c)

Fig 51. *Dependence of magnetization saturation on the fraction of the magnetic phase (a) $BaFe_{12}O_{19}$ - $BaTiO_3$, (b) $SrFe_{12}O_{19}$ - $BaTiO_3$, (c) $Ba_3Co_2Fe_{24}O_{41}$ - $BaTiO_3$*

This in an indication that magnitude of magnetization saturation follows the tendency of the sum property. The average magnetization in the composite is the result the simple diluting trend with no effect of the ferroelectric phase. Apparently, it proves that the magnetic properties originating from a short-order strong magnetic interactions are practically insensitive to the presence of ferroelectric phase, as it was stated in the Introduction (Chapter 1.1.4.).

Some words must be said regarding the composition $BaFe_{12}O_{19}$ 10% - $BaTiO_3$ 90%. As we can see in Fig. 52 (the hysteresis is given at a larger scale), the curve is deflected from the expected behavior (dashed line). Such a behavior, increasing at some point the value of the coercive field could be, in principle, connected to the presence of the third phase in the composite. Unfortunately, the XRD data for 10% - 90% compositions is not available at the moment to confirm this conclusion.

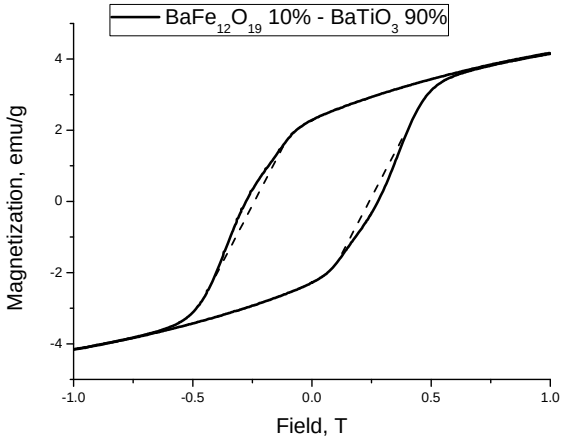

Fig 52. *Magnetization hysteresis of $BaFe_{12}O_{19}$ 10% - $BaTiO_3$.90%*

Comparing the values of the coercive fields in the composites we see that the coercivities first decrease and then increased with decreasing fraction of magnetic phase in the compositions $BaFe_{12}O_{19}$ - $BaTiO_3$ and $SrFe_{12}O_{19}$ - $BaTiO_3$. Opposite is observed for the $Ba_3Co_2Fe_{24}O_{41}$ - $BaTiO_3$ composition. It is known that larger grains decrease the coercive force. Keeping in mind SEM images for the latter composition, we could say that such behavior could be one of the consequences of the phase agglomeration. In fact the value of the coercive field for the 10% - 90% composition is very close to the one of the pure phase (7,8 *mT* and 6.72 *mT*, respectively). The result obtained for $BaFe_{12}O_{19}$ - $BaTiO_3$ and $SrFe_{12}O_{19}$ - $BaTiO_3$ samples (including nonmonotonic behavior) can be due to the change in the magnetic anisotropy and partial alignment of the magnetic moments in the 50%-50% compositions.

The temperature dependence of the magnetization was expected to reveal some anomalies near the phase transition temperatures of the ferroelectric phase (183 to 203 K and 273 K). Such a behavior could be one of the indications of the magnetoelectric effect. Namely, phase transitions in barium titanate are accompanied by deformation of the unit cell. This deformation would result in stresses in the magnetic phase, which via piezomagnetic effect could be transformed into magnetization. However, no anomalies were detected in this temperature range. The jumps in the dependence for $SrFe_{12}O_{19}$ 50% - $BaTiO_3$ 50% are connected to some faults in the system (short circuits) and must be considered as noise.

Very clear magnetic domain images obtained the compositions containing cobalt Z-ferrite, allowed to make an analysis of the dependence of the domain size on the amount of magnetic phase. The calculations were performed by means of WSxM 4.0 package. The average domain size could be extracted by plotting self-correlated images of the original file. The results are represented in Figs. 53-55.

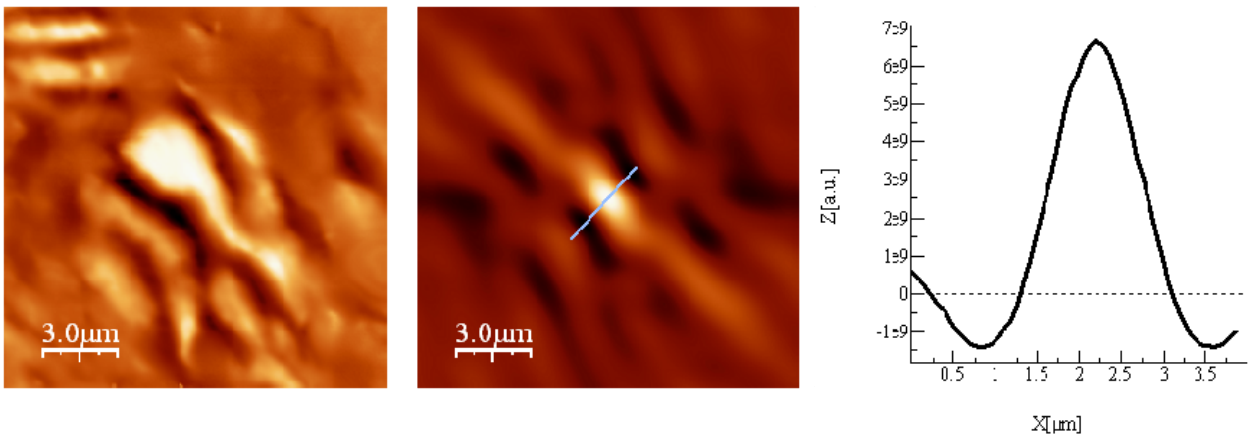

(a) (b) (c)

Fig 53. *Average domain size approximation for pure $Ba_3Co_2Fe_{24}O_{41}$ (a) MFM, (b) self-correlation image, (c) cross-section of the self-correlation image*

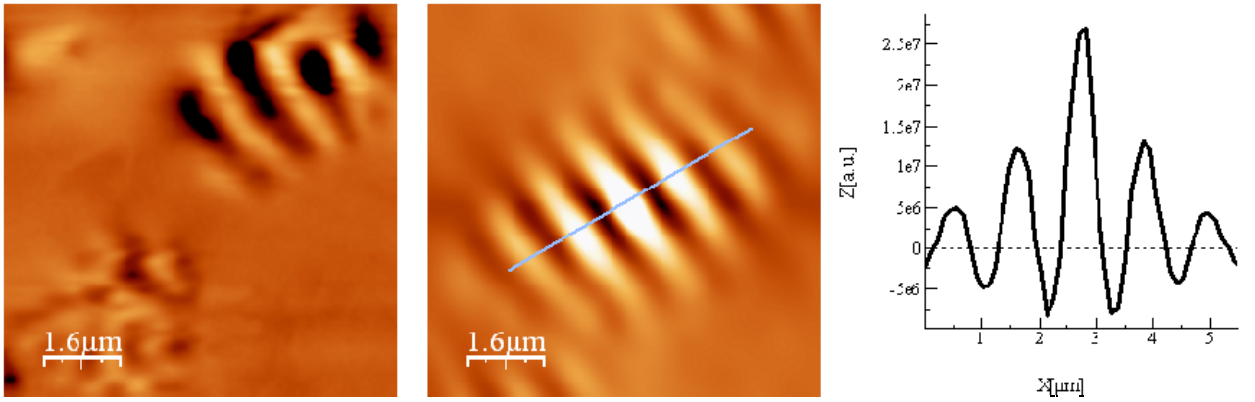

(a) (b) (c)

Fig 54. *Average domain size approximation for $Ba_3Co_2Fe_{24}O_{41}$ 50% - $BaTiO_3$ 50% (a) MFM, (b) self-correlation image, (c) cross-section of the self-correlation image*

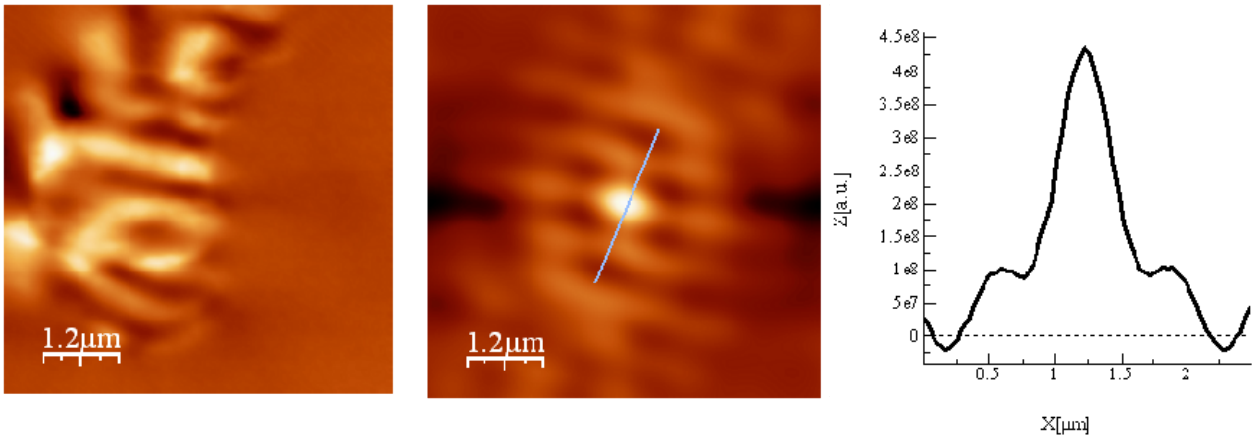

(a) (b) (c)

Fig 55. *Average domain size approximation for $Ba_3Co_2Fe_{24}O_{41}$ 10% - $BaTiO_3$ 90% (a) MFM, (b) self-correlation image, (c) cross-section of the self-correlation image*

The following values of the average domain size were extracted from the cross-section curves:

$Ba_3Co_2Fe_{24}O_{41}$ 100%	1.817 μm
$Ba_3Co_2Fe_{24}O_{41}$ 50% - $BaTiO_3$ 50%	0.75 μm
$Ba_3Co_2Fe_{24}O_{41}$ 10% - $BaTiO_3$ 90%	1.025 μm

Larger values of the domain size in the 10% - 90% composition comparable to the ones of the ones in composite with 50% of the ferrite phase could be another consequence of the partial ferrite phase agglomeration in this composition.

4.5. Ferroelectric properties

The vertical PFM images of all the samples showed preferred domain orientation. The polarization was always shifted towards negative values (polarization head terminated at the sample surface). Such phenomena (called self-polarization) could result from asymmetry of the sample (ferroelectric grain contacts the magnetic material and the air) internal field created at the surface due to incomplete screening and formation of double layers. This field is responsible for the partial (negative) orientation of surface domains.

The changes in the effective d_{33} coefficient as a function of composition were analyzed with WSxM 4.0 software by plotting histograms of the PFM images. The peaks in histograms can be extrapolated by the Gaussian fitting. In the case of composites, the fitting was done by plotting two Gaussian peaks: one with the maximum close to zero and the other with the maximum shifted towards negative values. The first peak corresponding to a signal close to zero is connected to the magnetic phase. The second peak is connected to the signal coming from the negatively polarized ferroelectric grains. The position of the maximum of the ferroelectric peak gives us the value of the effective piezoelectric coefficient d_{33}.

The histogram plots for all the studied compositions are given if Fig. 56

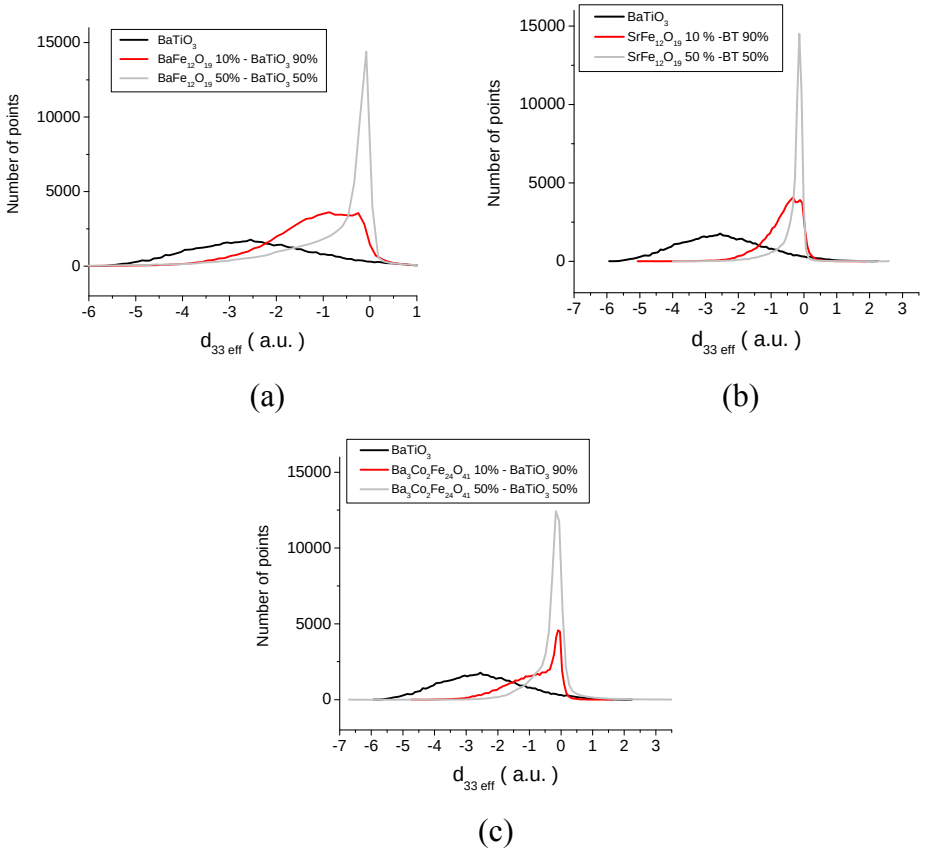

Fig 56. *Histograms of the vertical PFM images for (a) $BaFe_{12}O_{19}$ – $BaTiO_3$, (b) $SrFe_{12}O_{19}$ – $BaTiO_3$, (c) $Ba_3Co_2Fe_{24}O_{41}$ – $BaTiO_3$, together with the reference curve of pure $BaTiO_3$*

The results for the values of the effective piezoelectric coefficients are given in Table 5

	Percentage of ferrite	$d_{33\ eff}$, *a.u.*
$BaTiO_3$	-	2.59
$BaFe_{12}O_{19}$+$BaTiO_3$	10%	1.34
	50%	0.77
$SrFe_{12}O_{19}$+$BaTiO_3$	10%	0.74
	50%	0.35
$Ba_3Co_2Fe_{24}O_{41}$+$BaTiO_3$	10%	0.94
	50%	0.48

Table 5. *Effective piezoelectric coefficients vs. composition*

As we can see, the value of the effective piezoelectric coefficient decreases with increasing amount of a magnetic phase. Similar behavior was noted by S. Panteny *et. al*[61] in their report on barium titanate-silver composites. This could be also related to the fact that we measured surface (2D) piezoelectricity while the volume fraction (%) is related to a volume effect. The results of the analysis of the local hysteresis loops are summarized in Table 6.

	d_{33}, *a.u.*	V_C, *V*
$BaTiO_3$	240.1	6.34
$SrFe_{12}O_{19}$ 10% +$BaTiO_3$ 90%	34.4	8.33

Table 6. *Piezosignal saturation and coercive coercive voltage in barium titanate in comparison with the composition $SrFe_{12}O_{19}$ 10% +$BaTiO_3$ 90%*

As can be noted, the drastic fall in d_{33} saturation value is complemented with the increase of the coercive voltage in the composite sample. The latter was also reported in [61]. The increase in the coercive field might result from the interactions of the ferroelectric grains (mechanical clamping, or depletion effect) with magnetic grains. These interactions would hinder the domain wall motion when the electric field is applied.

It is hard to make a clear conclusion regarding the drastic fall of the value of polarization saturation in the composite compared to the one in the pure barium titanate phase. It can be related to the pronounced grain size effect commonly observed in $BaTiO_3$. On the other hand, lower quality of the ferroelectric material in co-sintered composite may contribute to this effect, too. It is also possible that high voltage applied via PFM may be enough to polarize several grains in $BaTiO_3$ but cannot propagate further in the composite sample.

4.6. Electromagnetic coupling

The experiment with local poling could answer the important question which mechanism is responsible for magnetoelectric coupling in a multiferroic composite sample. Local poling done on a single ferroelectric grain may exert mechanical stress on a magnetic grain and thus cause magnetoelectric interaction via electrostriction/piezomagnetic effect. Other interactions (e.g., modulation of surface charge density via field effect) are also possible. Similar experiment to observe local magnetoelectric coupling was performed by Zavaliche *et al.*[62]. They dealed with the epitaxial columnar nanostructures of $BiFeO_3/CoFe_2O_4$. After poling a large fraction of the magnetic columnar structures fully reversed their contrast from white to black, some partly changed color, and only a few remained unchanged. However, this result may be caused by the electrostatic effect due to a very fine grain sizes and polarization of the entire area comprising both ferroelectric and magnetic parts. The experiments with localized poling of a single grain were attempted for the first time and thus (if successful) can be a base for future studies in bulk and thin film magnetoelectric composites.

The experiment show that the full polarization reversal in the ferroelectric grain causes appreciable changes in the magnetic contrast, namely, the shift of the position of magnetic domain by more than 1 μm. Taking into account the fact that the domain size itself is of the same order this should lead to the variation of local magnetization of ≥50% of the initial value. Thus the local magnetoelectric effect can be very high reaching $\Delta M_r/E_c$ where ΔM is the variation of the magnetic moment. This effect may have various applications in the specially prepared nanostructures where the strain/stress transfer is facilitated by design and can be used for electrical writing/magnetic reading applications.

Further work is obviously needed to make a definitive conclusion on the nature of the effect observed in this work. In this respect the measurements of the macroscopic coupling are absolutely necessary to link the observed local effect with the macroscopic behavior.

5. CONCLUSIONS

In this work, we studied structural, microstructural, electrical and magnetic properties of novel multiferroic composites based on hexagonal ferrites ($BaFe_{12}O_{19}$, $SrFe_{12}O_{19}$ and $Ba_3Co_2Fe_{24}O_{41}$ (magnetic component) and $BaTiO_3$ (ferroelectric component). These were recently sintered for the first time in Imperial College (UK) by R. C. Pullar. The initial structural characterization was done by the XRD and EDS analysis and showed the absence of third phases (within the accuracy of used methods) with a clear separation and good mixing of the magnetic and ferroelectric phases. In compositions with low concentration of magnetic phase we found abnormally grown grains due to the agglomeration of the magnetic powder. It is hypothetized that such agglomeration is caused by the magnetic interaction between magnetic powders during mixing. Further characterization of their magnetic, dielectric and local ferroelectric properties has demonstrated sufficiently high magnetization and piezoelectric coefficients retained also in composites. Some deterioration of the properties of ferroelectric components was observed by PFM and attributed to the interactions of the ferroelectric grains (mechanical clamping, or depletion effect) with magnetic grains. Also, the size effect in $BaTiO_3$ may be involved. Magnetic domains were observed in all composites and domain size depended on the composition. The magnetization scaled linearly with the volume fraction of the magnetic phase in accordance with standard composite models. Dielectric properties of the composites showed a pronounced relaxation related to both high conductivity and Maxwell-Wagner effect and the ferroelectric phase transition temperature was unchanged as compared to bulk. Finally, a shift of the magnetic domain position was observed upon the application of sufficiently high voltage to the neighboring grain. This local magnetoelectric effect holds promise for future application of these composites in microelectronic devices.

General remarks and future work

In order to achieve a good performance of the magnetoelectric composites, it is not enough to have just remarkable individual properties of its components measured separately. One also needs to ensure sufficient performance of the parent phases and good connectivity between them. As it was observed in many other magnetoelectric composites, the properties of the ferroelectric component are most affected by the presence of the foreign phases during co-sintering, porosity and grain size effect. The same tendency was observed in presented work. This means that the direction of the further optimization of these composites should be first of all

aimed at improving their ferroelectric properties and connectivity of the phases. One should try to avoid mechanical stresses appeared in the composite which led to the deformation of the unit cell of the ferroelectric phase towards higher symmetry. But we should not forget that in the composite this would be not the only factor affecting the ferroelectricity. We must always take into account possible doping with magnetic ions and other defects which are much hardly to control in the composites compared to the single phase compositions. The other thing which could affect the ferroelectric properties is a formation of conductive channels of the magnetic phase, especially at high volume fraction of magnetic phase. In our 50%-50% composites the poling was not possible because of this problem. In future, the compositions of 70%-30% or 80%-20% must be used for further development. The attempts can be taken in order to improve the microstructure, at least to make the phase distribution more homogeneous. Especially it concerns the compositions with 10% fraction of the ferrites where agglomeration led to big grain sizes.

Speaking in general, every composite system is a very complex object to study. Properties of each individual phase cannot be considered separately anymore and the development of each phase affects another component. Therefore, the present work yields just initial results that will be helpful for the further optimization of the properties of multiferroic composites based on hexagonal ferrites.

6. REFERENCES

[1] C. W. Nan, *Phys Rev. B* **50**, 6082 (1994)

[2] H. Schmid, *Ferroelectrics* **162**, 665 (1994)

[3] B. K. Ponomarev *et al. , Ferroelectrics* **161**, 43 (1994)

[4] J. F. Scott, *Nature* **442**, 759 (2006)

[5] B. D. H. Tellegen 8 *Philips Res. Rep.* **3,** 81 (1948)

[6] J. van Suchetelene, *Philips Res. Rep* **27,** 28 (1972)

[7] G. Harsh, J.P. Dougherty, and R.E. Newnham, *Int. J. Appl. Electromagn. Mater* **4**, 145 (1993)

[8] M. I. Bichurin, I. A. Kornev, V. M. Petrov, and I. Lisnevskaya, *Ferroelecrics* **204**, 289 (1997)

[9] J. Rui, A. V. Carazo, K. Uchino, and H. E. Kim *Jpn. J. Appl. Phys*., Part 1 **40**, 4948 (2001)

[10] K. Mori and M. Wuttig, *Appl. Phys. Lett*., **81**, 100 (2002)

[11] C.W. Nan, L. Liu, N. Cai, J. Zhai, Y.Ye, Y. H. Lin, L. J. Dong, and C. X. Xiong, *Appl. Phys. Lett.* **81**, 3831 (2002)

[12] R. E. Newnham, D. P. Skinner, and L. E. Cross, *Mater. Res. Bull* **13**, 525 (1978)

[13] A. Y. Emelyanov, N. A. Pertsev, S. Hoffmann-Eifert, et al., *J. Electroceram.* **9**, 5 (2002)

[14] L. Mitoseriu and V. Buscaglia, *Phase Transitions* **79**, 12, 1095, Dec 2006

[15] X. Qi, J. Zhou, Z. Gui, *et al*., *Adv. Funct. Mater.* **14**, 920 (2004)

[16] H. K. Liu, J. H. Huang, C. W. Hsieh, *et al.*, *J. Mater. Sci.* **40**, 1979 (2005)

[17] K. K. Patankar, V. L. Mathe, A. N. Patil, et al., *J. Electroceram* **6:2**, 115 (2001)

[18] J. Ryu, A. Carazo, K. Uchino, et al., *J. Electroceram.* **7**, 17 (2001)

[19] A. Testino, L. Mitoseriu, V. Buscaglia, *et al.*, *J. Eur. Ceram. Soc.* **26**, 3031 (2006)

[20] V. Buscaglia, M. T. Buscaglia, M. Viviani, *et al.*, *J. Eur. Ceram. Soc.* **26**, 2889 (2006)

[21] J. C. Maxwell, *Electricity and Magnetism*, Vol 1, Clarendon, Oxford, 1892

[22] K. W. Wagner, *Arch. Elektrotechnol. (Berlin)* **2**, 37 (1914)

[23] G. Perrier and A. Bergeret, *J. Polymer Sci. B: Polymer Phys.* **35**, 9, 1349 (1997)

[24] C. W. Nan *et al*., *J. of Appl. Phys.* **103**, 031101 (2008)

[25] J. Zhai, N. Cai, Z. Shi, *et al*., *J. Phys. D: Appl. Phys.* **37,** 823 (2004)

[26] G. A. Smolenskii *et al*. *"Ferroelectrics and related materials"*, Gordon and Breach Science Publishers, New York, 1984

[27] D. J. Towner, T. J. Lansford & B. W. Wessels, *J. Electroceram.* **13**, 89 (2004)

[28] Raul Valenzuela, *"Magnetic ceramics"*, Cambridge University Press, 1994

[29] R. A. McCurrie *"Ferromagnetic material. Structure and properties"*, Academic Press Limited, University of Bradford, UK, 1994

[30] J. J. Went, G. W. Rathenau, E. W. Gorter, G. W. Van Oosterhout, *Philips Tech. Rev*. **13**, 194 (1951/52)

[31] R. S. Tebble, D. J. Craik *"Magnetic Materials"*, John Wiley & Sons Ltd., 1969

[32] R. C. Pullar *et al, J. Mat. Sci. Lett.* **17**, 973 (1998)

[33] R. C. Pullar, M. D. Taylor, and A. K. Bhattacharya, *J. Eur. Ceram. Soc.* **22**, 2039 (2002)

[34] X.-H. Wang *et al.*, *Mat. Chem. and Phys.* **77**, 248 (2002)

[35] C. Sürig, K. A. Hempel, and Ch. Sauer, *J. Magn. Mater*. **157/158**, 268 (1996)

[36] M. M. Hessien, M. M. Rashad, and K. El-Barawy *J. of Magnetism and Magn. Mat.* **320**, 336 (2008)

[37] R. C. Pullar, M. D. Taylor, and A. K. Bhattacharya, *J. of Mat. Sci.* **32**, 349 (1997)

[38] R. C. Pullar, S. G. Appleton, and A. K. Bhattacharya, *J. of Magnetism and Magn. Mat.* **186**, 326 (1998)

[39] G. Benito, M. P. Morales, J. Requena, V. Raposo, M. Vazquez, and J. S. Moya, *J. of Magetism and Magn. Mat.* **234**, 65 (2001)

[40] T. Ogasawara and M. A. S. Oliveira, *J. of Magnetism and Magn. Mat.* **217**, 147 (2000)

[41] W. Zhong, W. Ding, N. Zhang, J. Hong, Q. Yan, and Y. Du, *J. of Magnetism and Magn. Mat* **168**, 196 (1997)

[42] J. Ding, W. F. Miao, P. G. McCormick, R. Street, *J. of Alloys and Compounds* **281**, 32 (1998)

[43] R. C. Pullar, A .K. Bhattacharya, *Mat. Res. Bull* **36**, 1531 (2001)

[44] J. Jeong, K. W. Cho, D. W. Hahn, B. C. Moon, Y. H. Han, *Mat. Lett.* **59**, 3959 (2005)

[45] G. Xiong, G. Wei, X. Yang, L. Lu, and X. Wang, *J. Mat. Sci*. **35**, 931 (2000)

[46] C. R. Brundle, C. A. Evans, Jr., and S. Wilson *"Encyclopedia of Materials Characterization"*, Butterworth – Heinemann, 1992

[47] FullProf User's Guide, *http://sinq.web.psi.ch/sinq/doc/fullprof_old.html*, retrieved 08.10.08

[48] K. H. J. Buschow and F. R. de Boer *"Physics of Magnetism and Magnetic Materials"*, Kluwer Academic Publishers, 2004

[49] A. L. Kholkin, I. K. Bdikin, V. V. Shvartsman, and N. A. Pertsev, *Nanotechnology* **18,** 095502 (2007)

[50] A. L. Kholkin, S. V. Kalinin, A. Roelofs, and A. Gruverman "*Scanning Probe Microscopy: Electrical and Electromechanical Phenomena at the Nanoscale"* eds. S. Kalinin and A. Gruverman, Springer, Berlin, 2006

[51] M. Abplanalp *"Piezoresponse scanning force microscopy of ferroelectric domains"*, ETHZ (Switzherland), PhD Thesis, 2001

[52] R. C. O'Handley *"Moderm magnetic materials"*, John Wiley & Sons, Inc., 2000

[53] Y. Martin and H.K. Wickramasinghe, *Appl. Phys. Lett.* **50**, 1455 (1987)

[54] NT-MDT, *http://www.ntmdt.com*

[55] S. Hong, J. Woo, H. Shin, J. U. Jeon, and Y. E. Pak, *J. Appl. Phys.* **89**, 2 (2001)

[56] Chang-Dae Oh *et al.*, *Integrated Ferroelectrics* **87**, 77 (2007)

[57] B. K. Chougule *et al.*, *J. Mater. Sci.* **42**, 10250 (2007)

[58] Devan *et al.*, *J. of. Alloys and Compounds* **461**, 678 (2008)

[59] A. K. Jonscher, Dielectric relaxation in solids (Chelsea Dielectrics, London, 1983).

[60] Z. Yu and C. Ang, *J. Appl. Phys.* **91**, 794 (2002)

[61] S. Panteny, C. R. Bowen, and R. Stewens, *J. Mater. Sci.* **41**, 3845 (2006)

[62] F. Zavaliche *et al.*, *Nanoletters* **5** , 1793 (2005)